arXiv:astro-ph/0205247v1 15 May 2002

To appear in the Astronomical Journal, August 2002

Crossing the 'Yellow Void' – Spatially Resolved Spectroscopy of the Post–Red Supergiant IRC+10420 and Its Circumstellar Ejecta[1]

Roberta M. Humphreys[2], Kris Davidson, and Nathan Smith[2]

Astronomy Department, University of Minnesota, Minneapolis, MN 55455

roberta@aps.umn.edu

ABSTRACT

IRC +10420 is one of the extreme hypergiant stars that define the empirical upper luminosity boundary in the HR diagram. During their post–RSG evolution, these massive stars enter a temperature range (6000-9000°K) of increased dynamical instability, high mass loss, and increasing opacity, a semi–forbidden region, that de Jager and his collaborators have called the "yellow void". We report HST/STIS spatially resolved spectroscopy of IRC +10420 and its reflection nebula with some surprising results. Long slit spectroscopy of the reflected spectrum allows us to effectively view the star from different directions. Measurements of the double–peaked Hα emission profile show a uniform outflow of gas in a nearly spherical distribution, contrary to previous models with an equatorial disk or bipolar outflow. Based on the temperature and mass loss rate estimates that are usually quoted for this object, the wind is optically thick to the continuum at some and possibly all wavelengths. Consequently the observed variations in apparent spectral type and inferred temperature are changes in the wind and do not necessarily mean that the underlying stellar radius and interior structure are evolving on such a short timescale. To explain the evidence for simultaneous outflow and infall of material near the star, we propose a "rain" model in which blobs of gas condense in regions of lowered opacity outside the dense wind. With the apparent warming of its wind, the recent appearance of strong emission, and a decline in the mass loss rate, IRC +10420 may be about to shed its opaque wind, cross the "yellow void", and emerge as a hotter star.

Subject headings: stars:atmospheres — stars:evolution — stars:individual(IRC+10420) — stars:supergiants

---

[1]Based on observations made with the NASA/ESA *Hubble Space Telescope*, obtained at the Space Telescope Science Institute, which is operated by the Association of Universities for Research in Astronomy, Inc., under NASA contract NAS5-26555.

[2]Visiting Astronomer, Kitt Peak National Observatory (KPNO), National Optical Astronomy Observatory , which is operated by the Association of Universities for Research in Astronomy, Inc., under cooperative agreement with the National Science Foundation.

1. Introduction

IRC +10420 may be one of the most important stars in the HR diagram for understanding the final stages of massive star evolution. With its high luminosity of $L \sim 5{\times}10^6\ L_\odot$ (Jones et al. 1993, Paper I) and extraordinary mass loss rate of $3 - 6 \times 10^{-4}\ M_\odot\ \mathrm{yr}^{-1}$ (Knapp & Morris 1985; Oudmaijer *et al.* 1996; Humphreys *et al.* 1997), IRC+10420 is one of the few known stars that define the empirical upper luminosity boundary in the HR diagram at intermediate temperatures, between the main sequence and the red supergiant region (see Figure 9 in Humphreys & Davidson (1994) and Figure 14 in this paper). The evolutionary state of these cool hypergiants is not obvious; they may be evolving toward the red supergiant region or back to the blue side after having lost considerable mass as red supergiants. As one of the warmest known OH masers and one of the brightest 10–20 μm IR sources in the sky, together with its A-F–type spectrum and visible ejecta (Humphreys *et al.* 1997, Paper II), IRC +10420 is an excellent candidate for post-red supergiant evolution.

It has been variously described in the literature as either a true supergiant (Humphreys *et al.* 1973; Giguere, Woolf & Webber 1976; Mutel *et al.* 1979) or a proto-planetary/post-AGB star (Habing, Hekkert, & van der Veen 1989; Hrivnak, Kwok, & Volk 1989; Bowers & Knapp 1989), depending on distance estimates that ranged from 1.5 to 7 kpc. In Paper I we combined multi-wavelength spectroscopy, photometry, and polarimetry to confirm a large distance of 4–6 kpc and the resulting high luminosity mentioned above. We showed that its large optical–IR polarization and color excess are mostly interstellar, not circumstellar. These conclusions were later supported by Oudmaijer *et al.* (1996) who demonstrated from CO data that IRC+10420 has to be much more luminous than the AGB limit. In Paper I we concluded that IRC +10420 is a post–red supergiant evolving back toward the blue side of the HR diagram, in an evolutionary phase analogous to the proto-planetary/post-AGB stage for lower mass stars. de Jager (1998) has suggested that most if not all of the intermediate temperature hypergiants are post–red supergiants. In their blueward evolution these very massive stars enter a temperature range (6000–9000°K) of increased dynamical instability, a semi-forbidden region in the HR diagram, that he called the *"yellow void"*, where high mass loss episodes occur.

Our HST images of IRC+10420 (Paper II) revealed a complex circumstellar environment, with a variety of structures including condensations or knots, ray-like features, and semi–circular arcs or loops within $2''$ of the star, plus one or more distant reflection shells. A few other intermediate-temperature hypergiants such as ρ Cas and HR 8752 occupy the same region in the HR diagram, but IRC +10420 is the only one with obvious circumstellar nebulosity, making it our best candidate for a star in transition from a red supergiant possibly to an S Dor–type variable (LBV), a Wolf-Rayet star, or a pre-SN state. Moreover, its photometric history (Gottleib & Liller (1978), and our Paper I) and spectroscopic variations (Paper I and Oudmaijer *et al.* (1996); Oudmaijer (1998)) indicate that it has changed significantly in the past century.

Motivated by this background, we have obtained long–slit spectroscopy of IRC +10420 with the

Space Telescope Imaging Spectrograph (HST/STIS), supplemented by groundbased near-infrared spectra. The high spatial resolution of STIS (0.″05 to 0.″1) allows us to separate the spectrum of the central star from the spectra of the surrounding ejecta for studies of morphology, velocity structure, and composition. We find that the spectrum at each location in the ejecta is essentially that of a reflection or scattering nebula as expected, but some of the spectral details differ from those in the star. The reflected spectrum gives us some novel information about the stellar wind and the morphology of the ejecta.

In the next section we describe our HST/STIS observations and groundbased near-infrared spectroscopy, and in Section 3 we describe the optical spectrum of the central source, the lower resolution near-infrared data, and the subtle differences between the spectrum of the star and the inner ejecta. Our analysis follows in the next sections. In section 4 we measure velocities along the slit to assess the kinematics of the ejecta; we find a surprising lack of variation of the reflected Hα profile. In section 5 we summarize the implications for the central star and its wind, and the morphology of the ejecta. We demonstrate that the wind of IRC+10420 is opaque or nearly so, and show how this may account for the the mixed observations of both outflow and infall in its spectrum. In a final section we comment on the evolutionary state of IRC+10420 and compare it to the other well-studied yellow hypergiants in the context of de Jager's "yellow void".

2. The Observations and Data Reduction

We obtained long-slit moderate resolution HST/STIS spectra of IRC +10420 and its ejecta with a spatial sampling of 0.″05 per pixel. The effective resolution was somewhat worse than 0.″05. The $52'' \times 0.''1$ spectrograph slit was oriented along position angle 58.3° and located at two positions shown in Figure 1. Slit "position 1" was centered on the star and passed through the bright inner ejecta, a small knot to the northeast, and across one of the arcs. The slit centerline of "position 2" was 0.″42 from the star (measured perpendicular to the slit), roughly southeast of position 1, and passed through a bright knot east of the star and through the bright ejecta in the fan-like structure to the south and southwest of the star (see Paper II). We used moderate dispersion STIS gratings G430M and G750M at several tilts selected to cover the wavelength ranges 4560–5100 Å and 6500–8600Å. The resulting spectral resolutions range from 8000 to 9000 and 5800 to 7600 in the blue and red data respectively. These observations were all obtained on 1999 September 10 and the journal of observations is summarized in Table 1.

We used the STIS Instrument Development Team's IDL-based data reduction package (Lindler 1999), which includes the same basic steps as in the CALSTIS reduction package in STSDAS but has significantly better distortion corrections and rebinning techniques. The spectra were flatfielded and flux and wavelength calibrated. For the exposures at wavelengths longer than 7000 Å, additional flat fields were obtained during Earth-occultation to help correct for fringing. Cosmic rays were removed from data samples with multiple exposures, and corrections for terrestrial motion were applied to all of the spectra.

The STIS IDT reduction package is superior to the standard one for cases where high spatial resolution is desired, because it minimizes the wavy flux-calibration errors that occur in narrow extractions such as we use for the central star. Since each STIS CCD row extends approximately along the dispersion direction, an extracted spectrum of a localized spatial region conceptually amounts to the sum of a few CCD rows. However, because the dispersion direction is not precisely aligned with the rows, a "3-row extraction," for instance, is not merely one set of three rows across the detector. The local central row of the extraction must vary adaptively with column number or wavelength, using interpolation techniques to combine data from about four CCD rows at each wavelength. At some wavelengths the extraction center is close to the middle of a detector row, at others it is closer to the division between two rows. For point sources, too simple a technique gives different results for these two cases, leading to variations in the calculated flux level. The resulting sinusoidal pattern in apparent flux level can be disagreeably large (several percent) in data processed with the standard CALTSIS procedures, but is substantially less when the IDT package is used instead.

We also corrected another, less familiar calibration error that has usually been neglected in the past. For the spectrum of the central star we extracted an unusually narrow sample, only 3 rows ($0\farcs15$ wide), from each two-dimensional STIS spectral image. When such narrow extractions of STIS data are reduced using the standard procedures, flux values for adjoining grating tilts disagree by 5–10% in the narrow wavelength overlap sampled by both tilts. This effect, which we discovered and assessed earlier in data on η Carinae, indicates a consistent error in the slope of the standard flux calibration for each grating tilt. It is caused by a variation in focus across the STIS detector, and becomes less conspicuous for wider extraction samples, i.e., in cases where poorer spatial resolution is acceptable. We therefore applied the appropriate corrections to the spectrum slope for each grating tilt, made minor corrections for small changes in pointing, and then "spliced" or merged the data from the two blue and four red grating tilts.

Near-infrared spectra were observed with the Cryogenic Spectrometer (CRSP) on the KPNO 2.1-meter telescope and with the PHOENIX high resolution infrared spectrometer on the 4-meter, during June 2000 and are summarized in Table 2. The CRSP low-resolution spectra from 0.9 to 2.5 μm (IJHK) were obtained using a $0\farcs8$-wide slit aligned with the STIS slit at position angle 58°. The I and H bands required 2 separate grating tilts to cover the full wavelength range. The I and J band spectra were also observed at an offset position $5''$ south of the star at the same position angle, but no significant differences were apparent there. The seeing was typically $\sim1''$ on the photometric nights and the spectra were extracted from a $4''$–wide section of the slit centered on the central object. The spectra were sky subtracted by chopping along the slit, with offsets of 20 to $30''$. Telluric absorption lines were eliminated by dividing by the spectrum of HR 7396, after removing the hydrogen lines from the standard star's spectrum. The spectra were then flux calibrated using ν Her. Small corrections of the flux and wavelength were needed to merge adjacent spectral oders, similar to the adjustments made to STIS data as described earlier. Since the CRSP data typically have a 2-pixel spectral resolution of several hundred km s^{-1}, no useful kinematic

information is available from the near-infrared emission lines.

High-resolution PHOENIX observations of a few bright hydrogen emission lines were also made. The observing conditions were non-photometric, but IRC+10420 is bright enough that useful spectra were obtained with $\sim$1.″5 seeing. The 0.″6-wide slit was oriented at position angle 58°, and sky subtraction was accomplished by chopping along the slit, with offsets of 20 to 30″. To remove telluric absorption features, the spectrum of IRC+10420 was divided by the spectrum of Vega. Broad hydrogen absorption lines in Vega's spectrum were easy to fit and remove at high spectral resolution, typically a few to several km s^{-1}.

The details of the STIS spectroscopy of the central star and the inner ejecta and the recent near-infrared spectra are described in the next section. While these results and the subtle differences between the spectra of the star and the ejecta are of interest and important for understanding IRC +10420's complex wind, its variability, and processes in the ejecta, the most novel results and implications for IRC +10420 are discussed in sections 4, 5 and 6.

3. The Spectrum of the Central Star and the Inner Ejecta

The earliest spectrograms of IRC+10420 in the blue wavelength region showed the absorption line spectrum of a mid- to late F-type star of very high luminosity, with no obvious emission lines (Humphreys *et al.* 1973). Irvine (1986) was the first to report strong Hα emission plus the [Ca II] $\lambda\lambda$7293,7323 lines in emission;[3] previous spectra of the Hα region had shown no emission (Fix 1981). In Paper I we reported strong emission in the Ca II near–infrared triplet lines $\lambda\lambda$8498,8542,8662 and identified Fe II and [Fe II] emission lines in the red spectrum. Oudmaijer (1998) published a high resolution echelle spectrum covering the wavelength range 3800–10400 Å and identified many permitted and forbidden emission features, including some lines of relatively scarce elements such as scandium, vanadium, yttrium, and potassium. None of the ground-based observations just mentioned had good enough spatial resolution to reliably separate the central star from its ejecta.

To examine the spectrum of the star and its wind with practically no contribution from the ejecta, we extracted a spectrum just three rows wide in the STIS data, corresponding to $\sim$ 0.″15 along the slit. The spatial sample was thus about 0.″1 $\times$ 0.″15, corresponding to a projected size of 500 $\times$ 750 AU at the nominal distance of 5 kpc. From these data we deduced the star's total apparent flux by applying suitable throughput corrections. These included some factors omitted in most other STIS work, noted in Section 2 above.

Figure 2 shows the resulting flux–calibrated spectrum in our blue and red wavelength ranges. Uncertainties in absolute flux values are difficult to assess because they are mainly systematic,

[3]HST/STIS spectra directly give vacuum wavelengths, but we have chosen to quote the more familiar laboratory or air wavelengths here. Both forms are given in the tables where appropriate. All Doppler velocities quoted here are heliocentric. For IRC +10420, $V_{LSR} \approx V_{hel} + 17.5$ km s^{-1}.

arising in the data reduction and calibration process; ± 5% is a realistic estimate. Figure 2 also shows a satisfactory fit to the continuum, a simple parabola in this log-log plot. If we measure flux and wavelength in erg cm^{-2} s^{-1} Å^{-1} and Å, then this smooth continuum is specified by log $F_\lambda = -13.701, -12.925, -12.432$ at log $\lambda = 3.7, 3.8, 3.9$ respectively (λ = 5012, 6310, 7943 Å). Since it matches the observed values within the likely errors, there is no need to seek a more sophisticated fit at this time. In Figure 3, which shows the relative spectrum "normalized" to have continuum levels close to unity, we divided the observed spectrum by this simple log-log-parabolic continuum (rather than by a local continuum fit which would be less well defined).

3.1. The Energy Distribution of the Central Object

Available groundbased photometry and spectroscopy of IRC +10420 cover regions 1″–10″ across, and therefore include various fractions of the circumstellar nebula. In Paper II using the HST/WFPC2(PC) images we found that the central object accounts for less than 50% of the total apparent blue and visual-wavelength light. As one might expect for a reflection nebula, the ejecta appear bluer than the star. We have used our STIS data (Fig. 2) to estimate apparent magnitudes of the star over a wider wavelength range. As mentioned above, we sampled a 0.015-square-arcsec area and then applied suitable throughput corrections. For wavelengths not included in the observations we adopt the smooth continuum fit shown in Fig. 2. The results are listed in Table 3; likely errors are mostly systematic, informally about ±0.05 for each magnitude and for each difference (color). Groundbased observations show that IRC +10420 slowly brightened about a magnitude in the blue from 1926 to 1970 (Gottleib & Liller 1978), but its visual flux (Paper I) has remained essentially constant since then. Our more recent space-based measurements are consistent with little or no change since the last ground-based photometry in 1991.

IRC+10420 is a highly reddened object due both to its large distance and to an uncertain amount of additional circumstellar reddening. Assuming intrinsic colors appropriate for a late A to early F–type supergiant, the observed colors for the central star (Table 3) correspond to a visual extinction $A_V \approx 6.5$–7 mag. In Paper I we showed that its high polarization in the visual is interstellar, corresponding to a high interstellar extinction of 6–7 mag thus accounting for the observed color excess. However its large infrared excess indicates a large amount of circumstellar dust which should form at roughly 100 AU (0.″02) from the star. In Paper II we found that the visual optical depth τ due to absorption and scattering is about unity at $r \approx 1''$ (5000 AU). Thus we would expect $\tau \approx 50$ at 100 AU and the star should be invisible. To reconcile these inconsistencies, we suggested that either the dust is "patchy" or inhomogeneous, or else that we view the star's photosphere near the polar axis with only a modest amount of circumstellar extinction along our line of sight. We will return to questions concerning the geometry of IRC+10420's circumstellar ejecta in sections 4 and 5.

3.2. The Emission and Absorption Line Spectrum of the Central Object

IRC +10420 has a complex spectrum of absorption lines and permitted and forbidden emission lines dominated by strong emission from Hα, Hβ, the Ca II infrared triplet, and [Ca II], as shown in Figure 3. The Hα, Hβ, and permitted Ca II lines all have prominent double-peaked emission profiles with a stronger blue component. Figures 4 and 5 show these profiles for the central star from the STIS data. The measured velocity separation of the emission peaks for all four lines is 100 to 120 km s^{-1} with the central absorption at + 71.2 ± 1.3 km s^{-1} (heliocentric).[4] The velocities of the emission peaks with respect to the central absorption imply outflow or wind speeds of 50 to 60 km s^{-1}, somewhat higher than the expansion velocity of ≈ 40 km s^{-1} inferred from the OH maser and CO observations (Bowers 1984; Knapp & Morris 1985). In Paper I we attributed the double emission peaks to rotation of a hypothetical disk or ring, while Oudmaijer *et al.* (1994) suggested they might be due to a bipolar outflow. However, in Section 4 below we report a serious difficulty for either of these interpretations; these profiles most likely result, instead, from radiative transfer effects in the star's optically thick wind. The measured velocities for these lines are summarized in Table 4.

We first noted the extraordinarily broad wings of the Hα profile in Paper I. In the STIS data for the central star they are easily visible out to more than ± 1000 km s^{-1} for both Hα and Hβ (Fig. 4). In the relatively low-speed wind of IRC+10420, the most obvious explanation for these wings is scattering by free electrons. Their relative strength is reminiscent of η Car, suggesting that $\tau_e \sim 1$ in the region where the escaping Balmer photons originate (cf. Davidson et al. 1995, Hillier et al. 2001). In principle this reasoning can produce a new estimate of the mass loss rate, but calculations beyond the scope of this paper would be required. For that purpose one must know the intrinsic Hα luminosity corrected for extinction, and other details.

Similar broad wings may be present on the Ca II lines. For example, Ca II λ 8542 has a prominent blue wing (Fig. 5) which resembles Hα, while the red side is masked by Paschen absorption. The weaker Ca II λ8498 line may also have a faint blue-side wing, and the third member of the triplet, λ8662, was not included in our STIS observations. We also note that λ8498 is narrower than either of the brighter lines, λ8542 and Hα, and this may have some significance for models.

The Ca II emission lines are probably produced in the star's wind or envelope by radiative de-excitation from the strong Ca II H and K absorption upper levels. The [Ca II] emission lines however are not often seen in stellar spectra; their upper states would normally be collisionally de-excited back to the ground state. In Paper I we showed that about one-fourth of the excitations result in the observed [Ca II] lines and the electron density is roughly three times higher than the critical density. We have repeated that calculation with our high spatial resolution STIS data

[4]The systemic velocity is usually assumed to be +58–60 km s^{-1} (heliocentric), based on the OH and CO observations (Bowers 1984; Knapp & Morris 1985; Oudmaijer *et al.* 1996)

and confirm our previous estimate. The [Ca II] lines are thus produced in a region of much lower density than normally found in the atmospheres of even the most luminous normal A and F–type supergiants. Presumably these lines originate outside the dense the wind, at $r > 2R_{star}$ where $n_e < 10^8$ (see section 5 below).

In addition to the specific lines discussed above, numerous permitted and forbidden emission lines of ionized metals, including some relatively scarce elements, dominate the red spectra: Fe II, Ti II, Sc II, Y II, Cr II and [Fe II] and [V II]. Most of the identified absorption lines of the ionized metals such as Fe II, Ti II, Cr II and Sc II plus others are observed at blue wavelengths, but strong absorption lines of O I, N I and the Paschen lines are easily visible in the far red specta (Fig. 3). The general appearance and relative strengths of the emission and absorption lines in our STIS spectrum of the central star are consistent with the echelle spectrum published by Oudmaijer (1998). Our measured velocities for the emission and absorption lines are summarized in Tables 4 and 5, and agree well with the velocities for the same lines reported by Klochkova, Chentsov & Panchuk (1997) and Oudmaijer (1998). Thus the STIS data provide confirmation that groundbased results were not misleading due to contamination by the ejecta.

The Spectral Type: The first low resolution spectrogram of IRC +10420 showed the features of a very luminous mid- to late F–type star, with a G band and strong Ca II H and K lines (Humphreys *et al.* 1973). However, the absorption lines in recent higher resolution digital spectra indicate a much earlier spectral type and therefore a warmer apparent temperature. Oudmaijer (1998) has compared the strengths of the absorption lines in the wavelength range 4690–4935 Å in his 1994 echelle spectrum to several supergiants with spectral types ranging from A2 to F8, and concludes that the lines are most consistent with an F0 to A2 type and may even be earlier than A2. Both the appearance and equivalent widths of the absorption lines in our STIS data agree with Oudmaijer's measurements. Thus there does not appear to have been any major change in the 5 years between the two spectra. We caution, however, that a spectral type inferred from a high-resolution echelle spectrum is not the same thing as an MK spectral type based on a low-resolution photographic image tube spectrum. Since many of the features used in the low resolution MK classification are resolved in the echelle spectrum, these spectral types are not based on the same features. In this connection, however, Klochkova, Chentsov & Panchuk (1997) estimated a temperature of 8500 °K, appropriate for a middle A-type supergiant, based on a simple atmosphere analysis of spectra from 1992–96. Furthermore, the equivalent widths of the absorption lines plus the presence of a weak G band, and the Ca I λ4226 line in a moderate resolution echelette spectrum from 1988 (Paper I) indicate a late A to early F-type star of high luminosity. So it appears that the apparent spectral type of IRC +10420 changed from a mid/late F-type to as early as a middle A type between 1970 and 1990. This change in spectral type and by implication a corresponding temperature increase, may not be due to evolution, but may instead reflect variations in its wind. This possibility is discussed more fully in section 5.

Line Identifications: Oudmaijer (1998) gives an exhaustive line identification list in his on-line table. We confirm his identification of Fe I (multiplet 60) in emission, but not the three [Fe I]

(multiplet 14) lines at $\lambda\lambda$7172,7388,7452. Instead we suggest that these are [Fe II] (multiplet 14) and that the entry in his table is a typographical error. He has also identified [O I] emission at $\lambda\lambda$6300,6363, in a wavelength region not covered by our STIS spectra. Additional absorption lines in his table in those other wavelength regions include Y II, V II, Sr II, Si II, Mg II and some neutral metals, Si I, Mg I and possibly even He I λ5876; however, no other He I lines are observed including λ10830, see section 3.5.

Although we see most of the lines identified by Oudmaijer in the wavelength ranges that we observed, some lines in our STIS spectra are either not apparent in his groundbased spectra or were not included in his table of identifications. In Table 6 we list some possible additional line identifications with their measured equivalent widths and velocities, and in Table 7 we list the unidentified lines in our STIS spectra. We used the revised multiplet line identification table (Coluzzi 1993) available at the Astrophysics Data Center (Catalog 6071A) and the emission line identification list for η Carinae by Zethson (2001). We calculated the vacuum and air wavelengths for the lines in Tables 6 and 7 using our mean velocities of the absorption lines of the ionized metals (86.2 $\pm$ 8.5 km s^{-1}) and of the permitted and forbidden emission lines (66.6 $\pm$ 8 km s^{-1}) in Table 5. With $\sim$ 8 km s^{-1} rms scatter about the mean velocity, the calculated wavelengths may be uncertain by as much as 0.2 Å. Some of these unidentified lines are potentially interesting, and several are relatively strong, such as the two lines near 7000 Å.

Inverse P Cygni Profiles: Oudmaijer (1995) reported that many of the ionized metal lines have emission and absorption on their *blue* and *red* sides respectively, but not all of the ionized metallic lines have profiles of this type. We confirm the presence of inverse P Cyg profiles in wavelength regions sampled both by our data and by Oudmaijer's, although in some cases either the emission or absorption is doubtful in our spectra. Our measured mean velocities are +40 $\pm$ 7 km s^{-1} and +107 $\pm$ 7 km s^{-1} for emission and absorption components, respectively. The velocities of absorption components differ by about 20 km s^{-1} from Oudmaijer's (1998) published velocities for the same lines, in contrast with the overall good agreement for "normal" absorption and emission lines. Oudmaijer (2002) also finds variability in the velocities from the inverse P Cygni profiles. This variability might be due to the changes in the relative strengths of the emission and absorption components, although in our spectra the emission components are rather weak in most of the profiles and the absorption profiles are usually symmetric, suggesting that they have not been distorted by the emission. Therefore we suspect that the velocity changes indicate variability in the outflow and infall of the material. In our data the inverse P Cygni emission component is blueshifted 27 km s^{-1} with respect to the mean velocity from the normal ionized metallic emission lines, consistent with the interpretation that these lines are due to infalling gas. In contrast the absorption component has a velocity 20 km s^{-1} larger than or redshifted with respect to the mean velocity of the ionized metal absorption lines in the rest of the spectrum (see Table 5).

In section 5 we discuss the kinematics of IRC+10420's wind and ejecta and propose a model that accounts for the apparent contradiction of both infall and outflow.

3.3. Spectra of the Bright Inner Ejecta

IRC+10420's circumstellar nebula is a reflection nebula. However, when we examined the spectra of the brightest ejecta, within 1″ of the star, we did notice some spectral differences which may be useful for understanding the processes in IRC+10420's wind and its immediately surrounding ejecta.

The central source is so bright at our longest wavelengths that photon scattering in the STIS CCD degrades the spectra of the ejecta in slit position 1. This scattered light problem is most obvious longwards of 8000 Å, but would compromise any equivalent width measurements for the ejecta beyond 7000 Å at this slit position. For this reason, we restrict our discussion of the ejecta spectrum to two locations on slit position 2: (*a*) the bright ejecta in the "fan", 0.″45 south of the star, and (*b*) the bright knot to the east of the star (see Figures 1 and 12).

The spectra on the star and at the two offset positions are essentially the same except for a few absorption lines and an emission line at position *a* for which the differences are quite pronounced. The individual lines with their wavelengths, equivalent widths and atomic transitions are listed in Table 8. Four of the absorption lines, Fe II (multiplet 42) at $\lambda\lambda$4924 and 5018Å, Cr II (multiplet 30) at λ 4824Å and a strong unidentified line measured at λ6963Å (Table 7) are much stronger in the star with equivalent widths more than three times greater than in the reflection spectrum. The third line in the Fe II (42) series is just outside our spectral coverage. The other lines in Cr II multiplet 30 observed in our spectra are also stronger in the star's spectrum, but the effect is most pronounced for the strongest line in the series. Close inspection of the line profiles shows a raised continuum on either side of the these absorption lines, suggesting that emission may be responsible for the weaker absorption lines in the ejecta. One emission feature, the unidentified line measured at λ8105 Å (Table 7) is stronger at position *a* than in the star. The spectrum at position *b* does not show these differences and seems essentially identical to that of the star although the S/N is poor.

The behavior of the emission lines of K I at $\lambda\lambda$7665 and 7699 Å identified by Oudmaijer (1995) in his echelle spectrum with inverse P Cygni profiles is more subtle in our spectra. K I emission is not apparent in our STIS spectrum on the star itself (Figure 6), although the strong interstellar K I absorption lines and weak stellar absorption components are present. However, in the spectrum of ejecta at location *a*, 0.″45 from the star, K I emission is clearly present and easily seen above the continuum (Fig. 6). We are confident of the identification because our measured velocities for the three K I components (IS abs., em., stellar abs.) agree with Oudmaijer's groundbased measurements and the K I emission line velocity also agrees with the velocities for the other emission lines in IRC +10420 (Table 5).

Strong K I emission has previously been observed in the extreme red supergiant VY CMa (Wallerstein 1958), and weaker emission has been detected in several stars including the circumstellar gas shells of the M–type supergiants α Ori (Bernat & Lambert 1975, 1976), and μ Cep (Mauron 1997), and in the spectrum of the hypergiant star ρ Cas (Lobel 1997). K I has a very low

ionization potential of only 4 eV. and is expected to form in low temperature, low density regions. Wallerstein's (1958) comparison of the intensities of K I and Na I emission lines in VY CMa yielded a temperature of only about 700 °K for the region where the lines are formed, assuming they come from the same gas. We therefore suspect that this rare line is formed outside the dense wind of IRC +10420, e.g., 0.″45 or 2000 AU from the star as shown in Fig. 6. We therefore looked for K I emission at different locations along slit position 1, and found that the K I emission components become clearly visible above the level of the continuum at distances of 0.″2 and 0.″5 from the central star to the NE and SW respectively. Thus it appears that the K I emission is formed in circumstellar gas at distances of a 1000 AU and greater from the star. This is not unlike α Ori whose K I emission extends from 5″ to as far as 50″ or 700 to 7000 AU (Honeycutt et al 1980).

3.4. The Diffuse Interstellar Bands

Given the large distance, it is not surprising that there are many diffuse interstellar bands ("DIB's") in the spectrum of IRC+10420. Oudmaijer (1998) measured several bands and derived an approximate color excess (E_{B-V}) attributed to interstellar dust. We thought it worthwhile to measure the strengths of these bands in our spectra on and off the central star to look for any differences that might be attributed to spatial variation across the line of sight or to additional circumstellar reddening of the star. Using the W_λ/E_{B-V} ratios in Jenniskens & Désert (1994) we find mean E_{B-V} values of 1.84 ± 0.81 and 1.87 ± 1.3, respectively, for 13 DIB's in the stellar spectrum and for 11 at the position 0.″45 south of the star. We attribute the large error at the offset position to the lower S/N in the spectrum. These results are somewhat higher than Oudmaijer reported and imply an $A_v \sim 6.1$ mag, slightly lower than that inferred from the observed colors of IRC+10420 (see section 3.1). This does not necessarily mean that the difference is due to circumstellar reddening. The strength of the DIB's indicate extinction due to the diffuse interstellar medium and do not include contributions from molecular clouds along the line of sight, which can be significant for an object at the distance of IRC+10420. These results are therefore consistent with our earlier conclusion that most of the observed reddening of IRC+10420 is interstellar.

3.5. The Near–Infrared Spectrum

The low-resolution near-infrared spectrum of IRC+10420 in Figure 7 is dominated by emission lines of the Paschen and Brackett series of hydrogen and lines of low-ionization metals like Na I, Fe II, and Mg I. We see some significant differences compared to earlier spectra obtained at the same wavelengths. The lines of Na I and Mg I noted by Thompson & Boroson (1977) are all present in our spectra, plus the prominent Mg I line at 1.488 μm which was absent in their 1976 spectrum. The absence of this line was used to justify their suggestion that the Mg I and Na I emission was due to pumping by blue and UV photons from an optically thick region, a possible chromosphere. Numerous Fe II and [Fe II] lines are now observed while none were reported by Thompson & Boroson

(1977), and the Fe I line that they detected at 1.601 μm is absent in our more recent spectrum. Fix & Cobb (1987) identified lines of Fe II in their high dispersion spectra from June 1984 with intensities comparable to what we observe. It appears that the most significant changes in the strength of low-ionization metal lines in IRC+10420's near-infrared spectrum occurred between 1976 and 1984, consistent with the changes in apparent spectral type observed at optical wavelengths. Our line identifications are in Table 9.

CO bandhead emission at $\sim$2.3 μm may be present in Figure 7, but the spectra are somewhat noisy and these wavelengths overlap with the higher-order Pfund series of hydrogen. Higher quality spectra are needed to further investigate these lines. No hint of molecular hydrogen emission at 2.122 μm is seen in our spectra. Also, no He I lines are seen in Figure 7, which is relevant to changes in IRC+10420's spectral type and characteristic temperature described earlier.

Atomic hydrogen lines in IRC+10420's near-infrared spectrum have also shown significant variability. Early near-infrared spectra by Thompson & Boroson (1977) and Fix & Cobb (1987) showed the hydrogen lines in absorption. Oudmaijer *et al.* (1994) later discovered Brα, Brγ, and Pfγ in emission with the higher-order Brackett (i.e. Br 12 and Pa 11) in absorption in the mid-1990's. Our spectra confirm these results and also show the Paschen lines in emission up to Pa 9. Oudmaijer *et al.* (1994) noted that the near-infrared hydrogen emission line profiles were asymmetric, the Brγ and Pfγ showed inverse P Cygni profiles, and the redshifted emission peak seen in Hα was missing in these hydrogen lines. Our high-resolution spectra of a few H line profiles in Figure 8 do not show inverse P Cygni profiles, but are asymmetric; the emission peaks of all these lines are blueshifted. Fits to the line profiles did not yield satisfactory estimates of the centroid velocities because of the significant asymmetry. Instead, we measured the heliocentric velocity of each line by bisecting it at half the maximum intensity; the mean velocity is +36 $\pm$ 2.6 km s^{-1}, blueshifted by $\sim$ 22 km s^{-1} with respect to the presumed systemic velocity, similar to the results found by Oudmaijer *et al.* (1994). The velocity of the Brγ is about 5 km s^{-1} higher than the velocities for Brα and Pa β indicating that it may be formed deeper in the wind.

Finally, Figure 8 confirms the *absence* of He I λ10830 in the near-infrared spectrum. He I λ10830 should be the strongest line of this species if it is present, so its absence raises some doubt about the identification of the feature near λ5876 as He I (Oudmaijer 1995; Klochkova, Chentsov & Panchuk 1997). The non-detection of He I λ10830 at this time may be useful as a future benchmark if IRC+10420 continues to get warmer. This line was detected in other objects observed the same night and with the same grating tilt configuration.

4. Geometry of the Inner Ejecta and the Hα Profile

Aside from a few differences noted above, the ejecta show the spectrum of the star reflected by dust. Therefore, in effect *we can observe the star's spectrum from various directions.* This is potentially valuable because most models for IRC+10420 have invoked a circumstellar disk, or

bipolar outflow, or other departures from spherical symmetry, which can be tested by inspecting line profiles as functions of position along the slits.

To be confident that the observed locations represent a wide range of directions from the star, we need information about the three-dimensional distribution of the scattering material. Doppler shifts of the reflected spectrum can serve this purpose in a way explained below. The most suitable reference feature is the minimum in the bright double-peaked Hα profile. Figure 9 shows velocities of this feature measured at various locations; we used extractions 3 pixels wide for the inner samples, 5 pixels wide at radii between $1''$ and $1''.5$, and 10 pixels wide beyond that. Due to expansion (see below), apparent Doppler shifts tend to increase in each direction away from the star; two straight lines in the figure conveniently mark these trends for slit position 1.

A brief analysis shows the relation between apparent velocity and three–dimensional position. The apparent Doppler velocity seen in a dusty reflective condensation is

$$V_{obs} = V_0 + V_r + V_z,$$

where $V_0 \approx +74$ km s^{-1} is the value for the same spectral feature when the star's spectrum is observed directly, V_r is the outward velocity of the condensation away from the star, and V_z is the corresponding relative velocity component along our line of sight. For demonstration purposes, adopt some constant ejection speed V_r and consider only slit position 1 which includes the star. Let x, z be spatial coordinates centered on the star; the z-axis extends along our line of sight (z increases with distance) while the x-axis is parallel to the spectrograph slit (x increases toward the northeast). For a given observed location, we know x from its position along the slit and we calculate $V_z = V_{obs} - V_0 - V_r$. Then $V_x = \pm\sqrt{{V_r}^2 - {V_z}^2}$, which allows us to deduce $z = (V_z/V_x)x$. (See Davidson *et al.* (2001) for a more detailed application of this method to another object.)

Figure 10 shows a set of illustrative results in the xz plane, using three sample ejection speeds $V_r = 25$, 50, and 100 km s^{-1}. Here our viewpoint is to the left of the figure, and each set of two curves (northeast and southwest) shows the spatial loci corresponding to the linear velocity trends drawn in Figure 9. We expect to see mainly the near side of the nebula, since the optical thickness for visual-wavelength internal extinction by dust exceeds unity out to a radius of about $2''$ (Paper II); therefore the curves in Figure 10 seem qualitatively reasonable except near the center where they are not expected to be valid (cf. Fig. 9). For assumed values of V_r less than about 30 km s^{-1}, observed material on the northeast side extends implausibly far along the line of sight; while values greater than 80 km s^{-1} entail a similar difficulty on the southwest side. In other words, *the structure has a likely shape if V_r is between, roughly, 35 and 70 km s^{-1}.* This statement is independent of arguments based on line widths in the stellar spectrum (Section 3 above) and is consistent with the outflow velocities inferred from the CO and OH observations and from the separations of the hydrogen and Ca II double emission peaks.

Figure 11 shows the spatial distribution of the data points in Figure 9, assuming that $V_r = 50$ km s^{-1}. The uncertainties are too large for this to be a formal model, but Figs. 10 and 11 confirm two expected but crucial generalities: (1) The Doppler velocities are consistent with reflection in

an expanding nebula of the type envisioned in the past (e.g., in Paper II); and (2) the observed locations "see" the star from a wide range of directions, spanning at least a 90° angle. Slit position 2 further widens the range of viewpoints. Moreover, the southwest side appears to be a little closer to us than the northeast side, and if the configuration has bipolar symmetry to some extent, then its axis is most likely tilted roughly 65° relative to our line of sight, consistent with the model we proposed in Paper II.

At least one smaller-scale structure is obvious in Figs. 9 and 11: the apparent Doppler velocity trend is locally reversed between $+1\farcs2$ and $+2''$ NE, where slit position 1 crosses one of the arcs reported in Paper II. To investigate this more thoroughly we measured 3-pixel-wide samples (the hollow squares in the figures) and the trend remains consistent at that narrower sampling interval. The resulting feature in Fig. 11 probably indicates that the arc structure is more or less flat rather than jet-like or shell-like, and indirectly represents the spatial orientation of a cross-section.

4.1. The Surprisingly Uniform Hα Profile

We have measured the Hα profile at four locations along slit position 1 and two along position 2, shown in Figure 12; this line is bright enough to provide adequate signal/noise even at places where other spectral features are uncertain. Figure 13 shows the results along with the star's apparent Hα profile. The shape of the double-peaked profile is practically the same at every location, if we allow for some blurring by local velocity dispersions in the reflecting material. Most significantly, within the uncertainties, *at every location the difference between the two peaks agrees with the 122 ± 10 km s^{-1} measured for the Hα profile in the stellar spectrum.* This result conflicts with most proposed explanations for the double-peaked profile. For instance, if the peaks represent rotation in a circumstellar disk or torus as we suggested in Paper I, then their projected velocity difference should include a factor of sin θ where θ is the angle between the disk axis and the local viewing direction. Since the viewing direction varies considerably among the sampled locations, that model predicts an obvious variation contradicted by Figure 13. The same difficulty arises, perhaps even more so, for the polar outflow model suggested by Oudmaijer *et al.* (1994). In order to reconcile the observations with either type of axial model, one must hypothesize a geometrical distribution of observed points that seems unlikely in light of the preceding subsection above. *Therefore we conclude that the double-peaked line shape arises in a roughly spherical arrangement of circumstellar gas,* rather than an axially symmetric or seriously asymmetric configuration. In Section 5 we comment on likely reasons for the double peaked shape.

5. The Physical State of IRC +10420's Wind or Envelope

In this section we review the physical context for spectroscopy of IRC +10420, and we propose several new hypothetical phenomena. Two unusual circumstances are crucial: (1) the outer layers

of this object exemplify a form of the modified Eddington limit (Humphreys & Davidson 1984, 1994) and (2) as a consequence, its dense wind is probably opaque. Recent discussions by de Jager & Nieuwenhuijzen (1997); de Jager (1998); de Jager *et al.* (2001) and Lobel (2001) are broadly consistent with the views expressed below, but those authors were primarily concerned with less extreme objects such as ρ Cas and HR 8752, and hence did not emphasize the distinctions between a nearly-static photosphere and an opaque wind. Since we approach the topic from a different viewpoint, our emphasis and terminology differ from theirs and so do some of the physical processes.

5.1. An Opaque Wind

Davidson (1987) assessed the criterion for a stellar wind to be opaque in the continuum and, if it is opaque, the resulting photospheric temperature as a function of luminosity and mass-loss rate. The temperature range 6000–8500 K observed for IRC +10420 is rather special: Due to the behavior of opacity, *opaque wind photospheres automatically fall within this temperature interval for a wide range of mass loss rates.*[5] Given the usual estimates for IRC +10420's mass loss rate and wind velocity quoted in Section 1 above, its wind density parameter Q defined in Davidson (1987) is of the order of $10^{-4.8}$. According to Fig. 1 of that paper, this is large enough to make the wind opaque and to give it a photospheric temperature in the critical range.

Therefore *traditional static atmosphere models and spectral classification cannot safely be applied to this object.* Conventional "effective temperature" is ill-defined in this case and should be replaced by some other form of characteristic temperature (Davidson 1987; Humphreys & Davidson 1994). In principle the underlying star may have evolved farther "blueward" than the A–F spectral type suggests, since the observable features originate in the wind. *Spectroscopic variations observed in the opaque wind during the past 30 years represent changes in the wind parameters, and therefore do not necessarily indicate major evolution of the stellar radius and interior in that time.* (Proviso: These assertions assume that the current mass loss rate is at least $1.5 \times 10^{-4}\ M_\odot\ \mathrm{yr}^{-1}$, based on the published estimates which mostly represent long-term average values. IRC +10420's extreme time-averaged mass loss rate distinguishes it from the other two famous yellow hypergiants, ρ Cas and HR 8752.)

Emergent radiation at any particular wavelength is created at locations where $\sqrt{3(\tau_{sc} + \tau_{abs})\tau_{abs}} \sim 1$, if τ_{abs} and τ_{sc} are optical depths for absorption and for scattering by free electrons. Idealized pseudo-LTE calculations with $v_{wind} \approx 30$ to 60 km s^{-1} provide a fair working model – merely an initial guess – for the likely state of IRC +10420. The wind is translucent, $\tau_{sc} \approx 1$, at radius $R \approx 1.6{\times}10^{13}$ cm ≈ 1 AU, where $T \approx 9000$ K and $n_e \sim 10^{12}$ cm^{-3}. The Balmer continuum originates in this region

[5]This statement applies also to supernova photospheres and LBV or S Doradus eruptions. In a sense it plays the same role for winds that the Hayashi limit does for convective atmospheres.

because $\tau_{abs} > 0.2\tau_{sc}$ near the Balmer edge. At longer wavelengths $\tau_{abs} < 0.05\tau_{sc}$, so the emergent visual-wavelength continuum must be created in deeper layers. The "stellar surface" is best defined as the sonic point in the flow (cf. Davidson 1987, deJager 1998), presumably at some temperature above 9000 K. Absorption lines, on the other hand, may be formed around $R \approx 2.2{\times}10^{13}$ cm $\approx$ 1.5 AU where $\tau_{sc} \sim 0.1$, $T \sim 7000$ K, and $n_e \sim 10^{11.2}$ cm^{-3}. The energy densities of thermal gas, bulk motion, and radiation there are roughly 0.6, 6, and 10 erg cm^{-3} respectively; and, given the likely turbulent state in lower layers, we should not be surprised if the magnetic energy density is of the order of 0.1 erg cm^{-3} or conceivably larger. Outside this radius the wind becomes cool and transparent as the hydrogen recombines. This model is too simplified to quote in more detail, but it evokes the basic nature of the case. A proper self-consistent NLTE model would be far beyond the scope of this paper, especially since three-dimensional gasdynamic calculations are required as noted later.

The chief reason for the opaque wind is that this star's L/M ratio is dangerously close to the Eddington limit, in a non-trivial sense described below. Other factors help destabilize the outer layers, but L/M is of paramount importance. A good way to approach the problem is to combine various remarks made by Humphreys & Davidson (1994), de Jager (1998), and Lobel (2001), plus a few additional ideas.

Consider the probable evolution of a star with initial mass around 40 $M_\odot$. Despite substantial mass loss it can evolve to become a red supergiant. (30–50% more initial mass would entail LBV-like behavior that precludes the RSG stage.) Suppose that the red supergiant then loses enough mass to raise L/M above the classical Eddington limit. This does not cause immediate trouble, because the atmospheric opacity at low temperatures is far less than the Thomson scattering value normally applied in $(L/M)_{Edd} = 4\pi cG/\kappa$. (Violating this limit in the interior merely ensures vigorous convection.) However, when the star later evolves blueward away from the RSG part of the H-R diagram, ionization and opacity near the surface increase rapidly as the photospheric temperature rises above 6500 K; then the Eddington limit becomes applicable, other effects help to destabilize the atmosphere, and a terrific wind ensues. The star has reached de Jager's (1998) "yellow void" in the H-R diagram.

The *modified* Eddington limit is relevant here, i.e., temperature-dependent absorption must be included in the opacity and the absorption peak between 8000 and 12000 K decreases the limiting value of L/M. This assertion is more subtle than it appears at first sight. Humphreys and Davidson (1984, 1994) and de Jager (1998) recognized that absorption scarcely affects the traditional static-atmosphere Eddington limit, because atmospheric density decreases as the limit is approached, reducing the absorption opacity so that asymptotically one is left with only Thomson scattering. Hence the "modified Eddington limit" is really a hypothesis that instability occurs if L/M exceeds, say, 80 or 90 percent of $4\pi cG/\kappa$. In that case the relevant densities are high enough so that absorption does increase the effective value of κ. Then the maximum allowed L/M is appreciably less than one would expect from the usual formula. Moreover, unlike the classical limit, κ is temperature-dependent, which may help incite the instabilities. This line of thought originated

in connection with LBVs or S Doradus stars (see Section 5 of Humphreys & Davidson 1994), but reappears in de Jager's (1998) and Lobel's (2001) discussions of yellow hypergiants, albeit expressed differently. Those authors emphasize other considerations such as partial ionization and non-radial pulsation, but L/M is the essential parameter that makes these stars behave more violently than normal supergiants of lower luminosity.[6]

IRC +10420 is uniquely pertinent in several respects. It is close to the place in the HR diagram where the low-temperature edge of de Jager's "yellow void" intersects the empirical upper luminosity boundary (see Fig. 14), and it has a higher luminosity and mass loss rate than other known yellow hypergiants. In a sense this object vindicates the "modified Eddington limit" concept: its wind is dense enough so that temperature-dependent Balmer continuum absorption contributes substantially to the photospheric opacity, and it is manifestly unstable. In other words, its atmosphere did *not* become tenuous in an asymptotic approach to the classical Eddington limit. Is its L/M ratio large enough? For a plausible assessment, suppose that the effective average κ is about $1.2\kappa_{sc}$, and that an instability arises when $L/M \approx 0.9 \times (4\pi cG/\kappa) \approx 33000$; then the indicated mass would be about 15 $M_\odot$. The star would need to have lost roughly 25 $M_\odot$ of its original mass, consistent with estimates based on other considerations (see Papers I and II, and also Nieuwenhuijzen & de Jager 2000).

5.2. The Spectroscopic Connection

The structure of the wind should provide a link between spectroscopy and the star's evolutionary status. Unfortunately, the spectral features discussed in Section 3 and by previous authors have so far failed to give us a clear geometrical picture. Some of them appear almost paradoxical. Below we suggest a phase-change "rain" model, but let us approach the problem in stages.

First consider IRC +10420's absorption lines: where are they formed? Some are inverse P Cygni components, while others resemble features in a quasi-static atmosphere. Lines formed near or below the sonic point in this dense wind should be greatly broadened by Thomson (electron) scattering, but the observed absorption features are fairly narrow. Three possible interpretations are –

(1) Maybe the present-day mass loss rate is less than 10^{-4} $M_\odot$ yr^{-1}, violating the "proviso" mentioned earlier, so the wind is transparent after all. This recourse seems unattractive because the emission lines and rapid spectral changes suggest an extraordinarily dense wind.

(2) Conceivably the wind flows from only limited regions of the star's surface, reminiscent of the solar wind with its coronal holes. If so, then a relatively normal atmosphere might exist in the uncovered areas. This unconventional possibility is motivated by remarks in subsection 5.4 below.

[6]Shaviv (2000) has warned that the Eddington limit has been oversimplified in other, geometrical ways, as well, in the past.

(3) Or perhaps the absorption lines arise in the wind, e.g. at radii around 1.5 R_{star} as suggested above in connection with a simple semi-quantitative model. We adopt this as the provisional "best bet" choice.
– But then the absorption line velocities present a difficulty. If formed in a simple wind, they should have negative Doppler shifts relative to the systemic velocity of the star, but observations show that this is not the case. The inverse P Cygni absorption components are redshifted compared to their related emission, and most other, normal-looking absorption lines are redshifted by about 15–25 km s^{-1} compared to the OH and CO emission (see Section 3 above).

In principle the observed OH and CO line centers need not coincide with the star's systemic velocity as most authors have assumed; but even so, the absorption lines discussed in Section 3 are certainly not blueshifted by -20 to -60 km s^{-1} relative to the star as one would expect for this wind. Therefore, as Oudmaijer (1995) concluded from the inverse P Cygni lines, some sort of "infall" seems to dominate the absorption-line gas. He suggested that this is material ejected in the RSG phase, and which moved out a few hundred AU (or perhaps less) before falling back. Dust is expected to form at $r \sim 100$ AU, 10–20 years after ejection; so radiation pressure acting on the dust presumably makes infall difficult at larger radii. Velocities must be adjusted within fairly narrow limits to enable delayed infall, and why a significant fraction of the earlier wind should be falling back on the star at the present time is quantitatively unclear. High-mode radial pulsation might provide another explanation for simultaneous outflow and infall. However, we emphasize again that the spectrum is formed in a wind rather than a quasi-static atmosphere; so a radial pulsation model would need to explain why the local wind falls back promptly when the stellar surface recedes below it. Therefore both qualitative conjectures – delayed infall and radial-pulsation infall – seem unpromising to us. In the next paragraph we propose a different reason why infall may occur in the inner wind. This idea makes use of the special temperature range found there.

5.3. Outflow and Infall

Based on quasi-LTE precedent, one expects a phase change from ionized to atomic hydrogen to occur near radius 1.5 $R_{star} \sim 1.5$ AU, where T falls below 7000 K and $n_H \sim 10^{11.3}$ cm^{-3}. Inside that zone, radiation pressure nearly cancels gravity so other effects (see, e.g., de Jager 1998) can help radiation to accelerate the gas outward. However, outside the critical radius, opacity drastically falls as the electrons recombine; then radiation pressure can no longer compete with gravity and the net acceleration turns decisively inward. We doubt that the gas simply coasts out to the dust-formation distance from there, since few if any features show relative velocities as large as the pertinent escape speed, roughly 100 km s^{-1}. Instead, *conditions in the transition zone appear favorable for a phase-change instability which allows infalling material to coexist with outflow.* This idea is speculative but physically plausible. Consider a localized region that has the same pressure as its surroundings but slightly lower temperature and higher density, and therefore lower ionization. NLTE heating/cooling effects may induce thermal instability, but the novel circumstance here is

the *opacity decrease* in the low-ionization blob, which can thus experience a net inward acceleration (i.e., gravity dominates) while the surrounding lower-density, more ionized, higher-opacity gas is still being accelerated outward. In other words, we propose that less-ionized "droplets" form in the mostly-ionized gas, and fall back toward the star until they re-ionize. A terrestrial analogy is condensation of rain in an updraft within a cumulus cloud. We further suggest that some or most of the absorption lines form in the inhomogeneous, locally denser falling material. This would help explain the observed relative redshifts in the IRC +10420 spectrum and perhaps their variability in the inverse P Cygni profiles. NLTE ionization may allow continued outward acceleration of the lower-density gas flowing outward between the droplets.[7] Meanwhile the infalling blobs seem likely to create numerous localized shocks wherein temperatures briefly rise to 15000–20000 K. Magnetic fields may also play a role as we note later.

Unfortunately this scenario is extremely difficult to model quantitatively, and we doubt that any existing computer code can provide either a trustworthy demonstration or a disproof. The calculations will require NLTE ionization and excitation (especially for the $n = 2$ level of hydrogen), radiative transfer, and gas dynamics or even MHD in a conspicuously inhomogeneous wind. A one-dimensional approach cannot simulate the intrinsically three-dimensional "rain." All traditional-style atmosphere analyses (see Lobel 2001, de Jager et al. 2001, Nieuwenhuijzen & de Jager 2000, and refs. cited therein) therefore appear unsuitable for this case. Lobel's quantitative result, that the averaged adiabatic index Γ_1 can be low enough to cause instability in cool hypergiants, is relevant and suggestive but it offers little guidance for the detailed structure of a brisk dense wind like that of IRC +10420.

We offer some remarks concerning size scales in the "rain" zone. As noted above, that region is located around $R \sim 1.5R_{star}$ and the thickness of the ionization transition zone is expected to be of the order of $0.15R$. The two most obvious intensive dynamical parameters, the speed of sound w and net gravitational acceleration $g_{eff} \sim 0.5g$, suggest a likely order-of-magnitude size for an infalling blob or "droplet":

$$w^2/g_{eff} \sim 5{\times}10^{11} \text{ cm} \sim 0.02R.$$

This dimensional-analysis result is essentially the same as the scale height that a static atmosphere would have at the same radius. The proposed size is optically thick in the core of the Hα line (see below). The internal timescale for a blob (i.e., size/w) would be a few days and its infall-and-reionization lifetime is of order 10–50 days.

One might expect the double-peaked Hα, Hβ, and Ca II emission to provide clues to the structure of the wind. Our STIS observations show that at least the Hα profile appears more or

[7]The situation described here pictorially resembles an infall model proposed by Howk *et al.* (2000) for τ Sco, but the physical processes are quite different. Their instability results from line-driven acceleration in a hot stellar wind, while ours concerns the behavior of ionization and average opacity in a critical temperature range. We use the words "rain" and "droplets" specifically to connote a phase change. However, Fig. 1 of Howk et al. illustrates our model quite well if the text labels are suitably altered.

less the same from all directions, and therefore does not represent a circumstellar disc or ring or polar outflow as previously thought (Section 4 above). de Jager, Israelian, & Lobel (1997) found that an ensemble of turbulent shocks can produce a double-peaked Hα profile, but their example is much narrower and weaker than that observed in IRC +10420. Most of the Hα from this object emerges at blueshifts and redshifts around $\pm$60 km s^{-1}, well outside the thermal and turbulent width. The blue peak F_λ is at least 8 times the continuum level (Fig. 4), indicating an origin either in gas hotter than 20000 K, or else at radii of the order of $4R_{star}$, or a mixture of both high temperature and large overall extent. Thus it is not obvious whether the Hα emission originates in the localized inflow/outflow shocks mentioned above (reminiscent of the de Jager et al. case) or, alternatively, in an extended outflow zone at large radii. This ambiguity is enhanced by the fact that Hα is rather *weak* relative to the high mass loss rate assumed here. The total Hα luminosity[8] is roughly 2000 $L_\odot$, which in a nebular context would require a volume emission measure of the order of $10^{61.2}$ cm^{-3}. But this is tiny compared to the V.E.M. $> 10^{64}$ cm^{-3} that the wind would have if it were fully ionized; evidently the average ionization fraction must be quite low in the outer wind, $r > 1.5R_{star}$. Thus, both obvious possibilities – emission from many small hot shocked zones in the innermost wind where infall occurs, or else nebula-like emission from widespread parts of the outer wind – are much harder to assess than Hα production in a hotter, fully ionized wind. The very broad line wings (Fig. 4) give another clue: at least a substantial fraction of the Hα emission comes from regions with noticeable scattering by free electrons, i.e., with column densities between 10^{23} and 10^{24} cm^{-2}. As noted earlier this is probably not true for the absorption lines. In summary, the Hα problem remains murky and some quantitative details seem to contradict each other!

Why do the Hα, Hβ, and Ca II lines have double peaks? de Jager, Israelian, & Lobel (1997) do not clearly explain this result for their turbulent shock example. Our suggestion for IRC +10420 is that critical regions have large velocity gradients and relatively small thickness in the radial direction, allowing line photons to escape from their creation zones along the outward and inward directions but not sideways. This idea seems to fit well with the conjectured local shocks between infall and outward flow in a "rain" scenario. Its applicability in the outer regions, however, is less clear.

5.4. The possible importance of stellar activity

Finally, we note that magnetic fields and stellar activity (in the same sense as solar activity) may play a role in this story. Convection and turbulence can occur more easily and more violently near the upper luminosity boundary in the HR diagram, conceivably even in stars hotter than 10000 K if they are close enough to the Eddington limit. The case is strongest in the red supergiant

[8]Assumptions for this estimate: The measured equivalent width is 44 Å, and the intrinsic continuum energy distribution resembles a 9000 K black body with a luminosity of $10^{5.7}$ $L_\odot$.

stage. Star-spots, magnetic fields, and associated outflow are known to occur in RSG's such as α Ori and VX Sgr (see, e.g., Schwarzschild (1975); Gilliland & Dupree (1996); Kluckers *et al.* (1997); Uitenbroek *et al.* (1998); Lobel & Dupree (2000, 2001); Tuthill *et al.* (1997); Chapman & Cohen (1986); Triglio *et al.* (1998)). It would not be very surprising if such activity has large-scale dynamical importance in the most extreme cases. The very luminous cool supergiant VY CMa has ejected material in a few directional looplike structures, qualitatively reminiscent of solar prominences but immensely larger and more massive (Smith *et al.* 2001). Non-radial pulsation might provide an alternative origin for these structures, but this idea seems less appealing since they are narrow, few in number, and remarkably looplike in appearance. If dynamically significant turbulent/magnetic activity does occur, then one obvious question is: How long does it persist during post-RSG evolution? The same factors that make a yellow hypergiant surface unstable lend themselves to the generation of turbulence and magnetic fields.

Images of the IRC +10420 ejecta show numerous arcs, knots, and jetlike structures (Fig. 1 and Paper II) which indicate localized ejection events in seemingly random directions, analogous to VY CMa although the two morphologies are not identical. As mentioned in Section 4, the velocity trend across one of these arcs suggests a flat geometry – which would be unexpected if it was created by non-radial pulsations, but reasonable if it was shaped by a magnetic field. Located at radii from $0.5''$ to $2''$ (2500 to 10000 AU), these features were probably ejected between 400 and 1000 years ago. Although it is difficult to know how far the star had evolved at those times, at least the innermost features may have been formed after the star had ceased to be an extremely cool RSG (see Section 6 below). Nedoluha & Bowers (1992) have reported surprisingly strong magnetic fields of the order of 1 mG in the OH maser regions at $r \sim 7000$ AU. A conventional extrapolation inward ($B^2 \propto \rho^{4/3}$ or $B \propto r^{-2}$) would give $B \sim$ many kG at the current stellar surface, impossibly strong because the magnetic energy density would then exceed all other local energy densities by a huge factor. A field proportional to r^{-1}, on the other hand, would give a surface magnetic energy density comparable to the thermal energy density (Section 5.1 above).

Given the critical temperature range and general instability (Lobel 2001), we should not be surprised if dynamically significant convective/magnetic activity occurs above the surface of IRC +10420 in its currently observed state. The thermal energy of the inner wind described in Section 5.1 exceeds that of the solar photosphere by a factor of order 10^6 while v_{esc}^2 is smaller by a factor of 100, and the region is dynamically less stable than the solar photosphere and chromosphere. Major surface activity therefore seems possible or even likely. This idea does not conflict with the rough global isotropy of the outflow (Section 4.1 above), since the hypothetical sporadic events may be numerous and random in direction, consistent with observed structures in the ejecta. Observations have been too sparse to detect possible rapid variations in spectral details. In summary, the ejecta of VY CMa and IRC +10420 provide credible evidence that turbulent/magnetic activity may help to cause or at least shape ejection events in the most extreme cool supergiants. Quantitative models, however, would be even more difficult to construct than for the "rain" phenomenon proposed above.

Active magnetic fields, and also shocks like those proposed in Section 5.3, can accelerate

charged particles to non-thermal energies. Solar flares produce MeV particle energies and indirectly produce neutron fluxes (Forman *et al.* 1986; Ramaty 1986). Therefore nuclear processing in the surface layers might conceivably affect the abundances of rare elements in spectra of extreme supergiants such as IRC +10420 and VY CMa. This remark is intended merely as a speculation that needs quantitative assessment in the future.

6. Final Remarks – Crossing the Yellow Void

From our perspective the yellow hypergiants, hidden by their dense winds, may appear to be relatively stalled on the upper HR diagram in the temperature range 6000 – 8000°K. Nieuwenhuijzen and de Jager (1997, 1998) said that these objects were "bouncing" at the cool edge of the "yellow void", but that expression refers only to the wind or superficial outer layers of the star. If the intermediate type hypergiants are post–red supergiants on blueward evolutionary tracks, as we believe for IRC +10420, then their interiors or cores will continue to evolve, unconcerned with their external appearance. So how can a yellow hypergiant cross the yellow void?

With these apparent temperatures and their very high luminosities, the yellow hypergiants are in the dynamically unstable region in the HR diagram described in the previous section and experience high mass loss rates and discrete ejection episodes with even higher mass loss accompanied by spectroscopic and photometric variations. The historical and recent shell episodes observed in ρ Cas are examples (Bidelman & McKellar 1957; Beardsley 1961; Lobel *et al.* 2002). The very luminous F-type star Var A in M33, which now shows TiO bands (Humphreys, Jones & Gehrz 1987), is very likely an example of a similar but more extreme and much longer shell event. Figure 14 shows an HR diagram with the yellow void and the positions of IRC +10420 and Var A plus ρ Cas and HR 8752 from Israelian, Lobel, & Schmidt (1999) and the apparent temperature shifts corresponding to their recent spectroscopic variations. Unlike IRC+10420, HST/WFPC2 images of ρ Cas and the very similar hypergiant HR 8752 show no evidence for circumstellar material (Schuster *et al.* 2002). Thus HR 8752 and ρ Cas may have only recently encountered this unstable region in their blueward evolution. Furthermore, the normal mass loss rates for HR 8752 and ρ Cas are at least 10 times less than those reported for IRC +10420.

Our HST images of IRC+10420 provide us with a snapshot of its mass loss history and show evidence for several mass loss episodes. The outermost reflection arcs at $\approx 5''$ were ejected about 3000 years ago, undoubtedly when the star was a red supergiant as this is comparable to, or greater than, the time expected for a massive star star to evolve back to warmer temperatures from the RSG stage (Schaller et al 1992; Schaerer et al 1993) The complex structures closer to the star correspond to more recent high mass loss, possibly discrete, asymmetric events. In Paper II we showed that IRC +10420 experienced a high mass episode during the past 600 years shedding about 1 $M_\odot$ with a mass loss rate $\sim 10^{-3}$ $M_\odot$ yr^{-1}. IRC +10420 has undoubtedly been in this highly unstable region of the HR diagram for several years.

The time scales for post red supergiant evolution, especially at these high luminosities, are very uncertain, ranging from several hundred to a few thousand years (Schaller et al 1992; Schaerer et al 1993). Stothers & Chin (2001) have suggested a model in which these stars *appear* to make frequent rapid excursions across the HR diagram due to dynamical instabilities as red supergiants. Whether post red supergiant evolution is smooth and continuous or sporadic, the yellow hypergiants very likely remain in this unstable state until, due to interior evolution, the underlying surface, defined as the sonic point beneath the opaque wind, becomes sufficiently hot ($\geq 12000°$K) to shed its dense false-photosphere or opaque wind. The star would next be seen on the blue side of the void with a temperature of 12000–20000°K, possibly as a post-RSG LBV like the "less luminous" type in Figure 14 (Humphreys & Davidson 1994) and with a much reduced mass loss rate. In principle, if the wind is opaque enough, the underlying stellar surface *might* already be above 12000 K; we do not propose that this is the case, but mention the possibility as a reminder of the disconnection between spectrum and stellar radius when a dense wind exists.

In addition to its vigorous mass loss earlier, IRC +10420 has shown some dramatic changes during the past century and even during just the last 30 years. Its historical light curve shows that it brightened by a magnitude in the 50 years prior to 1970. This might be due to a shift in bolometric correction to warmer temperatures after a shell episode lasting decades similar to Var A, although most authors (Paper I, Oudmaijer et al 1986) have interpreted it as thinning of the circumstellar dust along the line of sight. Blöcker *et al.* (1999) show that a two-component dust shell model based on their near–infrared speckle–interferometry "can be interpreted as evidence of a termination of an enhanced mass loss episode 60 – 90 years ago", which interestingly corresponds to the onset of the visual brightening. Thus, it appears that a high mass loss episode ended only recently and that its mass loss rate, while still high, has declined during the past few decades. The apparent temperature of an opaque wind tends to increase as the mass loss rate decreases (Davidson 1987). With the apparent warming of its dense wind, the recent appearance of strong hydrogen emission, and a possible decline in its mass loss rate, we suggest that IRC +10420 may be *in transit across the semi-forbidden region of the yellow void.* However, we do not know whether it has just begun or is near the end of its passage. The latter is the more interesting possibility, and continued observations of this remarkable star in the next few decades may reveal its future evolution.

Support was provided by NASA through grant number GO-7304 from the Space Telescope Science Institute, which is operated by the Association of Universities for Research in Astronomy, Inc., under NASA contract NAS 5-26555. We are especially grateful to Kazunori Ishibashi for processing the HST/STIS spectra of IRC+10420 with the STIS IDT software. We also thank Rene Oudmaijer for his comments on the inverse P Cygni profiles, Kerstin Weis for useful discussions on the spectra of unstable massive stars, and Robert Lysak for conversations about the Sun and solar activity.

REFERENCES

Bernat, A.P. & Lambert, D.L. 1975, ApJ, 201, L153

Bernat, A.P. & Lambert, D.L. 1976, ApJ, 210, 395

Bidelman, W.P. & McKellar, A. 1957, PASP, 69, 31

Beardsley, W.A. 1961, ApJS, 5, 381

Blöcker, T., Balega, Y., Hofmann, K.-H., Lichtenhaler, J., Osterbart, R. & Weigelt, G. 1999, aap, 348, 805

Bowers, P. F. 1984, ApJ, 279, 350

Bowers, P.F. & Knapp, G.R. 1989, ApJ, 347, 325

Chapman, J.M., & Cohen, R.J. 1986, MNRAS, 220, 513

Coluzzi, R. 1993-99, *A Revised Version of the Identification List of Lines in Stellar Spectra (ILLSS) Catalogue*, Bull. Inf. Centre Donnees Stellaires, Vol. 43, p. 7

Davidson, K. 1987, ApJ, 317, 760

Davidson, K., Humphreys, R.M., Hajian, A., & Terzian, Y. 1993, ApJ, 411, 336

Davidson, K., Ebbets, D., Weigelt, G., o Humphreys, R.M. et al. 1995, AJ, 107, 1784

Davidson, K., Smith, N., Gull, T.R., Ishibashi, K., & Hillier, D.J. 2001, AJ, 121, 1569

de Jager, C. 1998, A&A Rev., 8, 145

de Jager, C., Israelian, G., & Lobel, A. 1997, A&A, 325, 714

de Jager, C. & Nieuwenhuijzen, H. 1997, MNRAS, 290, L50

de Jager, C.,Lobel, A., Nieuwenhuijzen, H. & Stothers, R. 2001, MNRAS, 327, 452

Fix, J.D. 1981, ApJ, 248, 542

Fix, J.D. & Cobb, M.L. 1987, ApJ, 312, 290

Forman, M. A., Ramaty, R., & Zweibel, E. G. 1986, in *Physics of the Sun, Vol II: The Solar Atmosphere* (ed. P.A. Sturrock; D. Reidel, Dordrecht), p. 249

Giguere, P.T., Woolf, N.J., & Webber, J.C. 1976, ApJ, 207, L195

Gilliland, R.L., & Dupree, A.K. 1996, ApJ, 463, L29

Gottleib, E.W. & Liller, W. 1978, ApJ, 225, 488

Habing, H.J., Hekkert, P. & van der Veen, W.E.C.J. 1989, in IAU Symposium 131, *Planetary Nebulae*, ed. S. Torres-Peimbert (Dordrecht:Reidel), 381

Hillier, D.J., Davidson, K, Ishibashi, K., & Gull, T.R. 2001, ApJ, 553, 837

Honeycutt, R.K., Bernat, A.P., Kephart, J.E., Gow, C.E., Sandford II, M.T. & Lambert, D.L. 1980, ApJ, 239, 565

Howk, J. C., Cassinelli, J. P., Bjorkman, J. E. & Lamers, H. J. G. L. M. 2000, ApJ, 534, 348

Hrivnak, B.J., Kwok, S., & Volk, K.M. 1989, ApJ, 346, 265

Humphreys, R.M. 2001, in *Eta Carinae and Other Mysterious Stars,* ASP Conf. Ser. 242 (ed. T.R. Gull, S. Johansson, & K. Davidson), p. 233

Humphreys, R.M., & Davidson, K. 1984, Science, 223, 243

Humphreys, R.M. & Davidson, K. 1994, PASP, 106, 1025

Humphreys, R.M., Jones, T.J., & Gehrz, R.D., 1987, AJ, 94, 315

Humphreys, R.M., Smith, N., Davidson, K., Jones, T.J. *et al.*1997, AJ, 114, 2778 (Paper II)

Humphreys, R.M., Strecker, D.W., Murdock, T.L., & Low, F.J. 1973, ApJ, 179, L49

Irvine, C.E. 1986, BAAS, 18, 961

Israelian, G., Lobel, A., & Schmidt, M. 1999, ApJ, 523, L145

Jenniskens, P., & Désert, F.-X. 1994, A&AS, 106, 39

Jones, T.J., Humphreys, R. M., Gehrz, R.D. *et al.*1993, ApJ, 411, 323 (Paper I)

Klochkova, V. G., Chentsov, E. L., & Panchuk, V. E. 1997, MNRAS, 292, 19

Kluckers, V.A., Edmunds, M.G., Morris, R.H., & Wooder, N. 1997, MNRAS, 284, 711

Knapp, G. R. & Morris, M. 1985, ApJ, 292, 640

Lindler, D. 1999, CALSTIS Refererence Guide (CALSTIS version 6.4; Greenbelt, MD: GSFC)

Lobel, A. 1997, Doctoral Dissertation, "Pulsation and Atmospherical Instability of Luminous F and G–Type Stars", Vrije Universiteit Brussels

Lobel, A. 2001, ApJ, 558, 780

Lobel, A. & Dupree, A.K. 2000, ApJ, 545, 454

Lobel, A. & Dupree, A.K. 2001, ApJ, 558, 815

Lobel, A., Dupree, A. K., Stefanik, G., Torres, G., Israelian, G., de Jager, C., Nieuwenhuijzen, H., & Ilyin, I. 2002, BAAS, 34

Mauron, N. 1997, A&A, 326, 300

Mutel, R.L., Fix, J.D., Benson, J.M. & Webber, J.C. 1979 ApJ, 228, 771

Nedoluha, G.E. & Bowers, P.F. 1992, ApJ, 392, 249

Nieuwenhuijzen, H., & de Jager, C. 2000, A&A, 353, 163

Oudmaijer, R. D. 1995, Doctoral Dissertation, "Evolved Stars with Circumstellar Shells", Rijksuniversiteit Groningen

Oudmaijer, R. D. 1998, A&AS, 129, 541

Oudmaijer, R. D. 2002, private communication

Oudmaijer, R. D., Geballe, T. R., Waters, L. B. F. M., & Sahu, K. C. 1994, A&A, 281, L33

Oudmaijer, R. D., Groenewegen, M.A.T., Matthews, H.E., Blommaert, J.A.D., & Sahu, K.C. 1996, MNRAS, 280, 1062

Ramaty, R. 1986, *Physics of the Sun, Vol II: The Solar Atmosphere* (ed. P.A. Sturrock; D. Reidel, Dordrecht), p. 291

Schaller, G., Schaerer, D., Meynet, G. & Maeder, A. 1992, A&AS, 96, 269

Schaerer, D., Meynet, G., Maeder, A. & Schaller, G. 1993, A&AS, 98, 523

Schuster, M. T., Humphreys, R. M., Smith, N., Halvorsen, M., Davidson, K. & Gehrz, R. D. 2002, in preparation

Schwarzschild, M. 1975, ApJ, 195, 137

Shaviv, N. 2000, ApJ, 532, L137

Smith, N., Humphreys, R. M., Davidson, K., Gehrz, R. D., and Schuster, M. T. & Krautter, J. 2001, AJ, 121, 1111

Stothers, R. & Chin, C-w 2001, ApJ, 560, 934

Thompson, R.I. & Boroson, T.A. 1977, ApJ, 216, L75

Triglio, C., Umana, G., & Cohen, R.J. 1998, MNRAS, 285, 529

Tuthill, P.G., Haniff, C.A., & Baldwin, J.E. 1997, MNRAS, 285, 529

Uitenbroek, H., Dupree, A.K., & Gilliland, R.L. 1998, AJ, 116, 2501

Wallerstein, G. 1958, PASP, 70, 479

Zethson, T. 2001, Doctoral Dissertation, "Hubble Space Telescope Spectroscopy of Eta Carinae and Chi Lupi" , Lund University

This preprint was prepared with the AAS LaTeX macros v5.0.

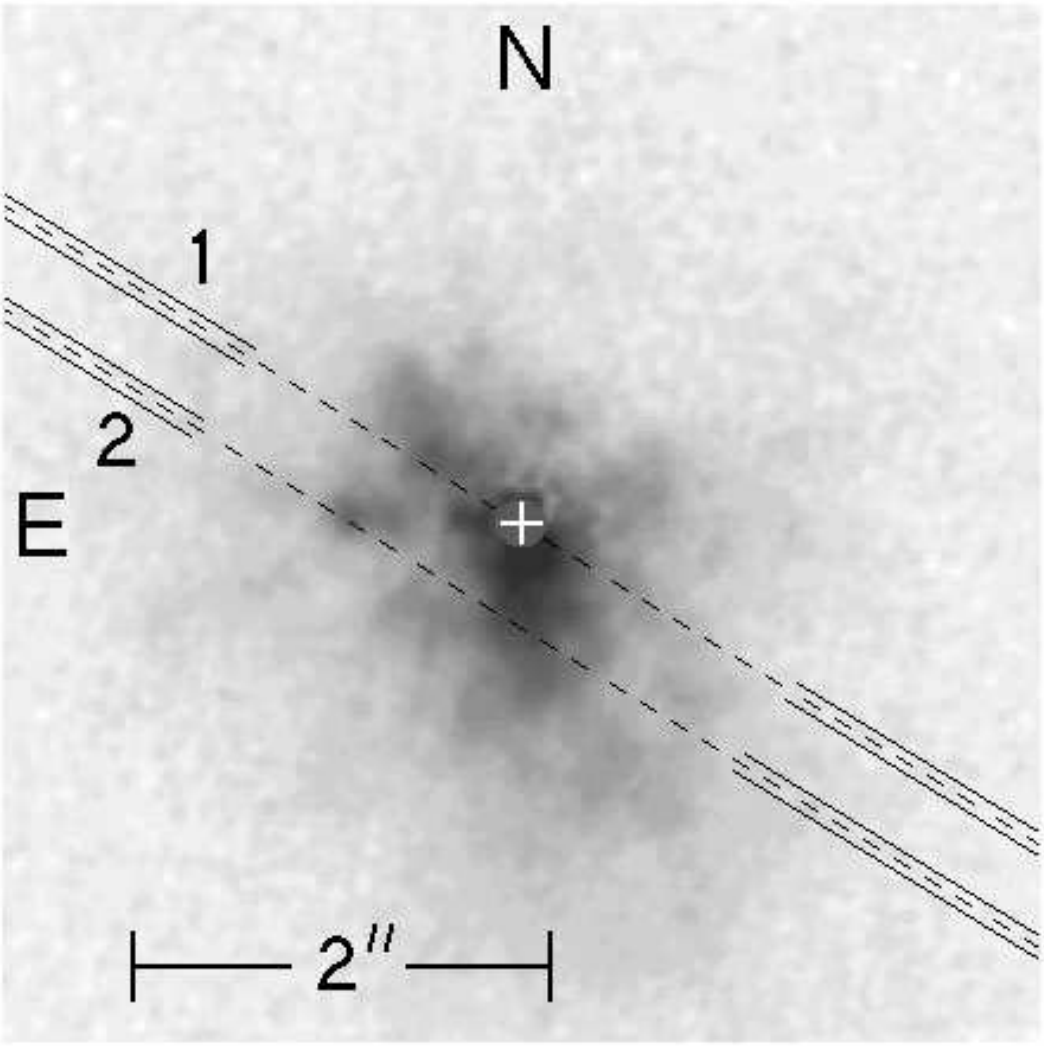

Fig. 1.— Positions of the two HST/STIS slits on the IRC +10420 WFPC2 image from Paper II.

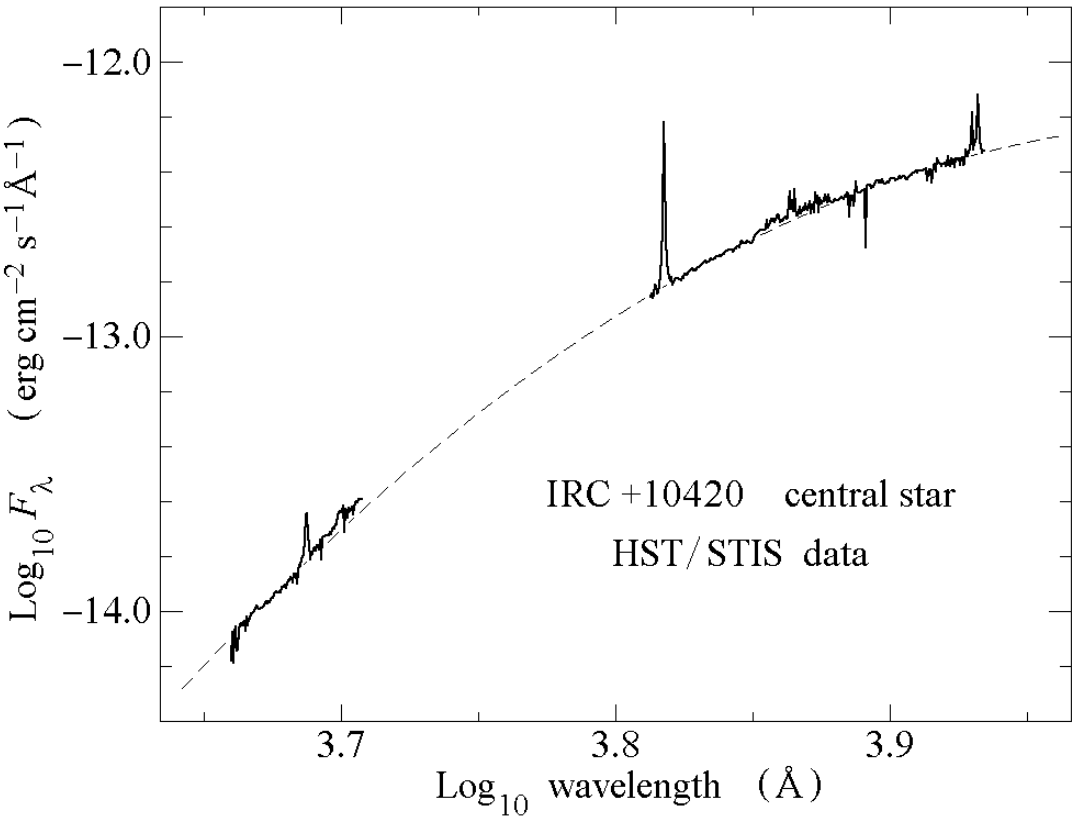

Fig. 2.— The flux calibrated spectrum of the central star with the parabolic fit to the continuum.

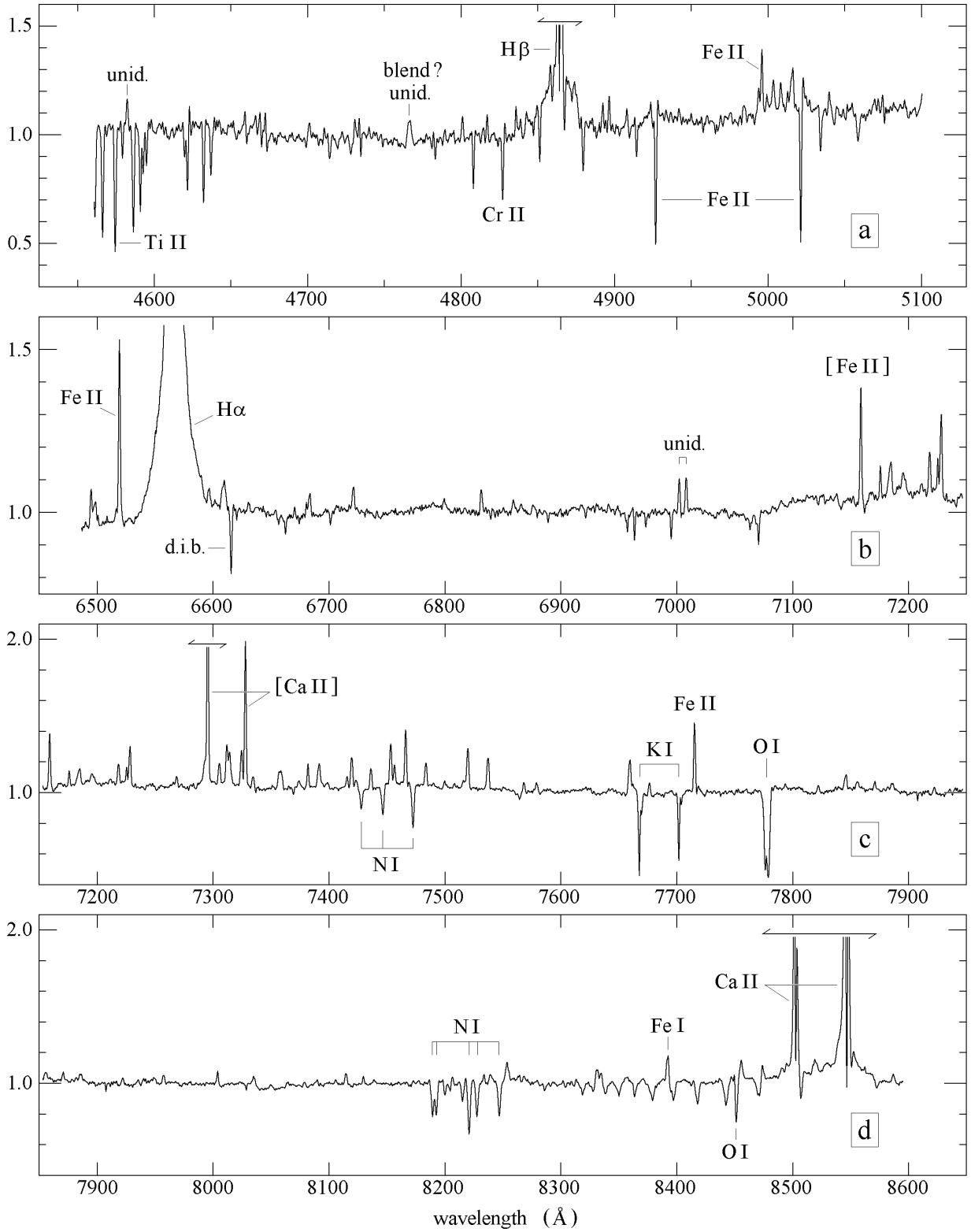

Fig. 3.— The normalized blue and red spectra of the central star with some of the stronger lines identified.

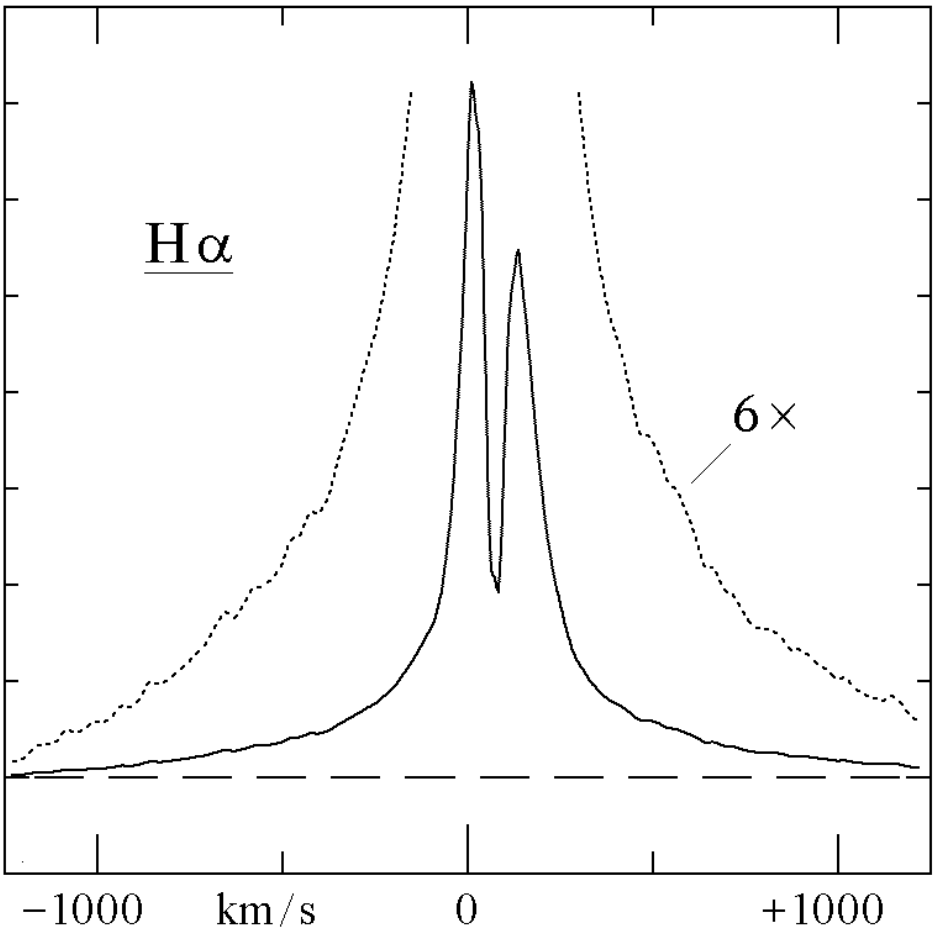

Fig. 4.— The profile of the Hα emission line showing the broad electron scattering wings projected against a 6× enlargement of the inner profile.

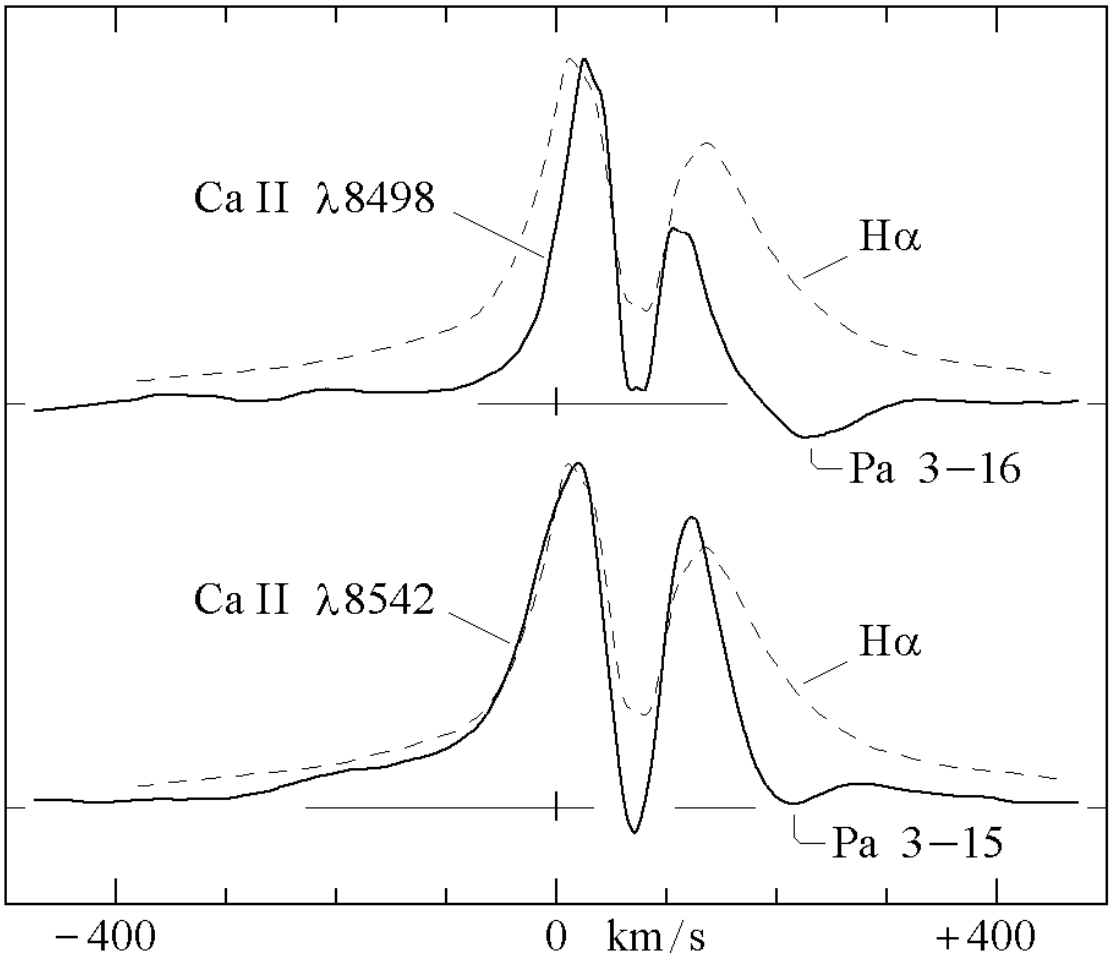

Fig. 5.— The split emission line profiles of the two Ca II lines at λ8498 and λ8542 compared with the Hα profile.

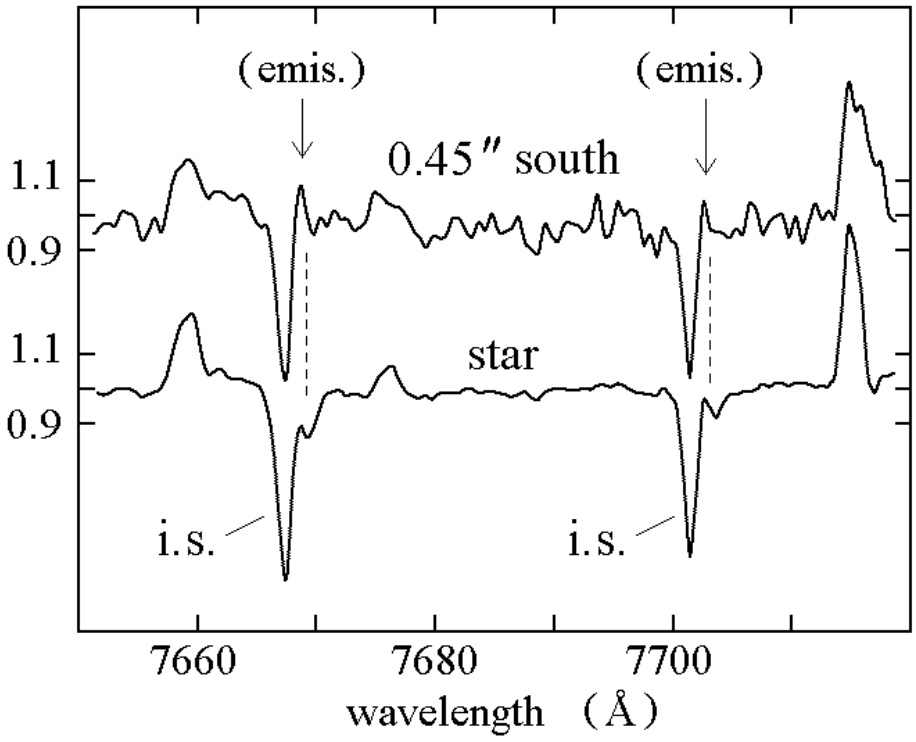

Fig. 6.— The wavelength region showing the K I emission lines. The strong interstellar K I absorption line and the K I absorption in the star are also identified. The lower panel shows the spectrum on the central star and the upper panel shows the same wavelength region in the ejecta at offset position $\underline{a}$ (Figure 12). The K I emission is clearly present above the continuum level in the ejecta.

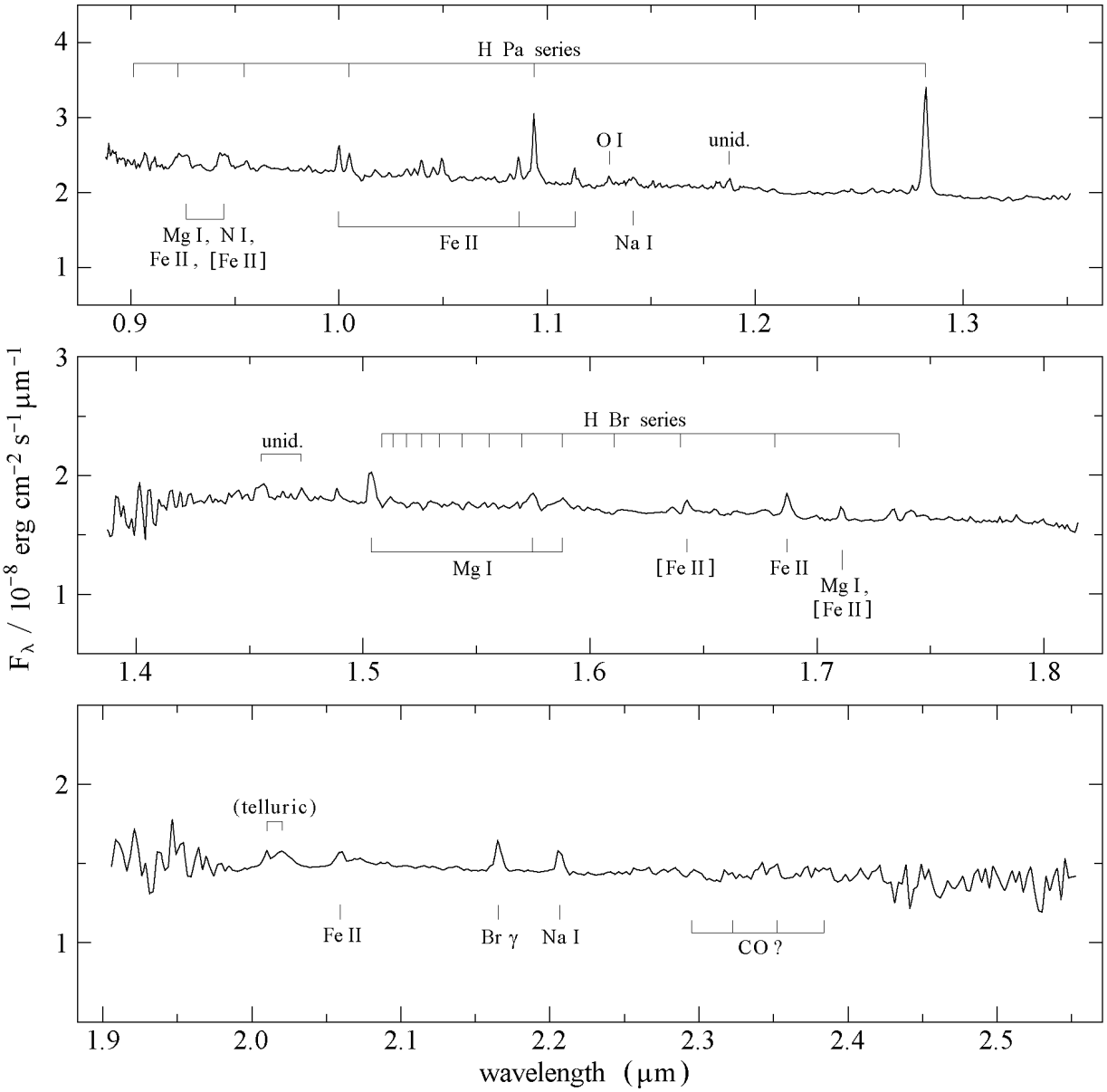

Fig. 7.— Low-resolution near-IR spectrum of IRC+10420 observed with CRSP on the KPNO 2.1m telescope. The signal to noise is worst at the edges of each bandpass, especially in the K-band, due to poor atmospheric transmission and filter cut-offs. In this figure "unidentified" means the resolution is inadequate to choose among several possibilities.

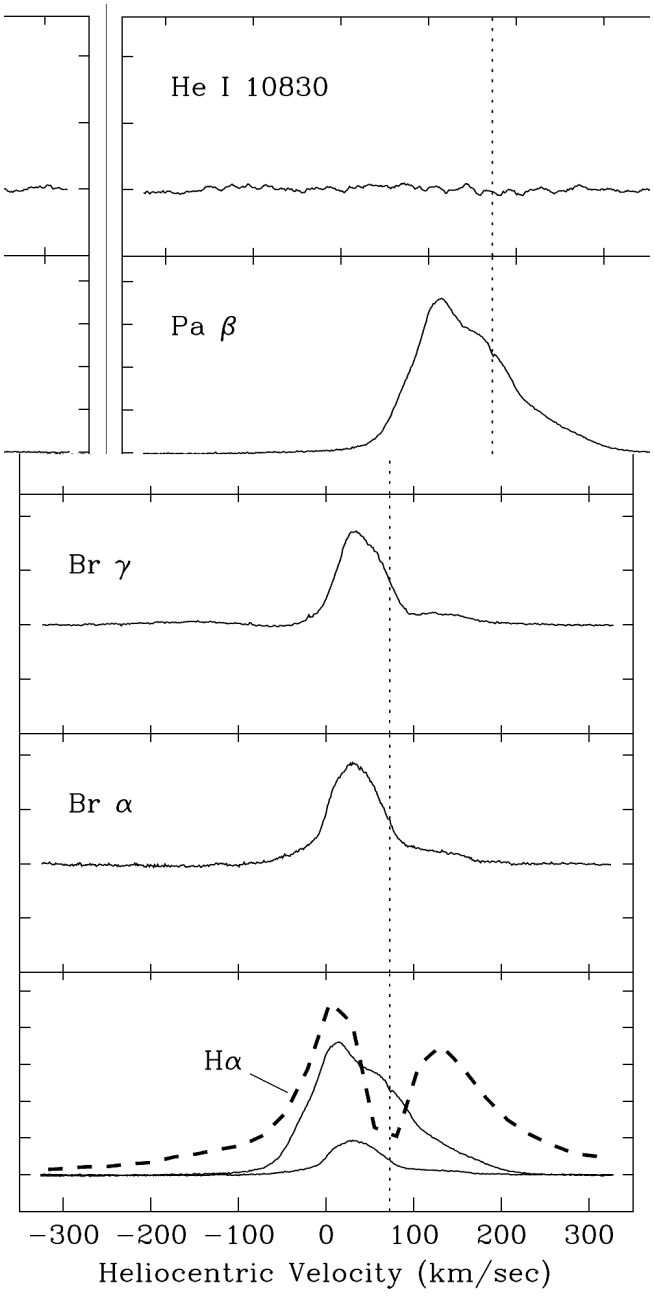

Fig. 8.— Line profiles of near-IR emission lines observed with PHOENIX on the KPNO 4m telescope. The presumed heliocentric radial velocity of +73 km s^{-1} is shown by the dotted vertical line in each panel. The bottom panel compares near-IR hydrogen line profiles observed with PHOENIX to the Hα profile of the central star observed with HST/STIS (dashed line)

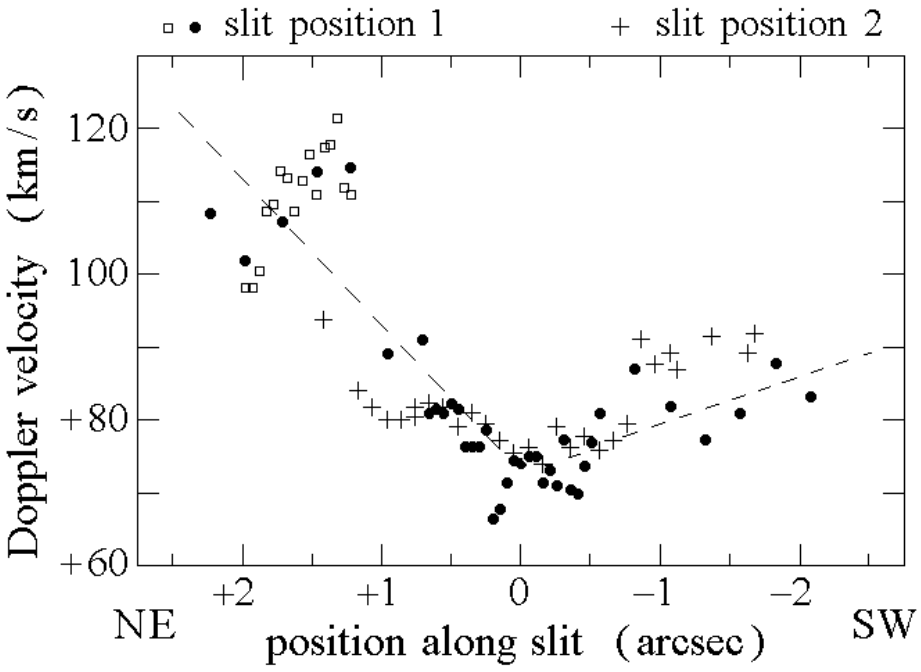

Fig. 9.— The measured velocities along the two slit positions. The measurements along slit positions 1 and 2 are shown as filled circles and crosses respectively. The open squares are the measurements across the arc at slit position 1.

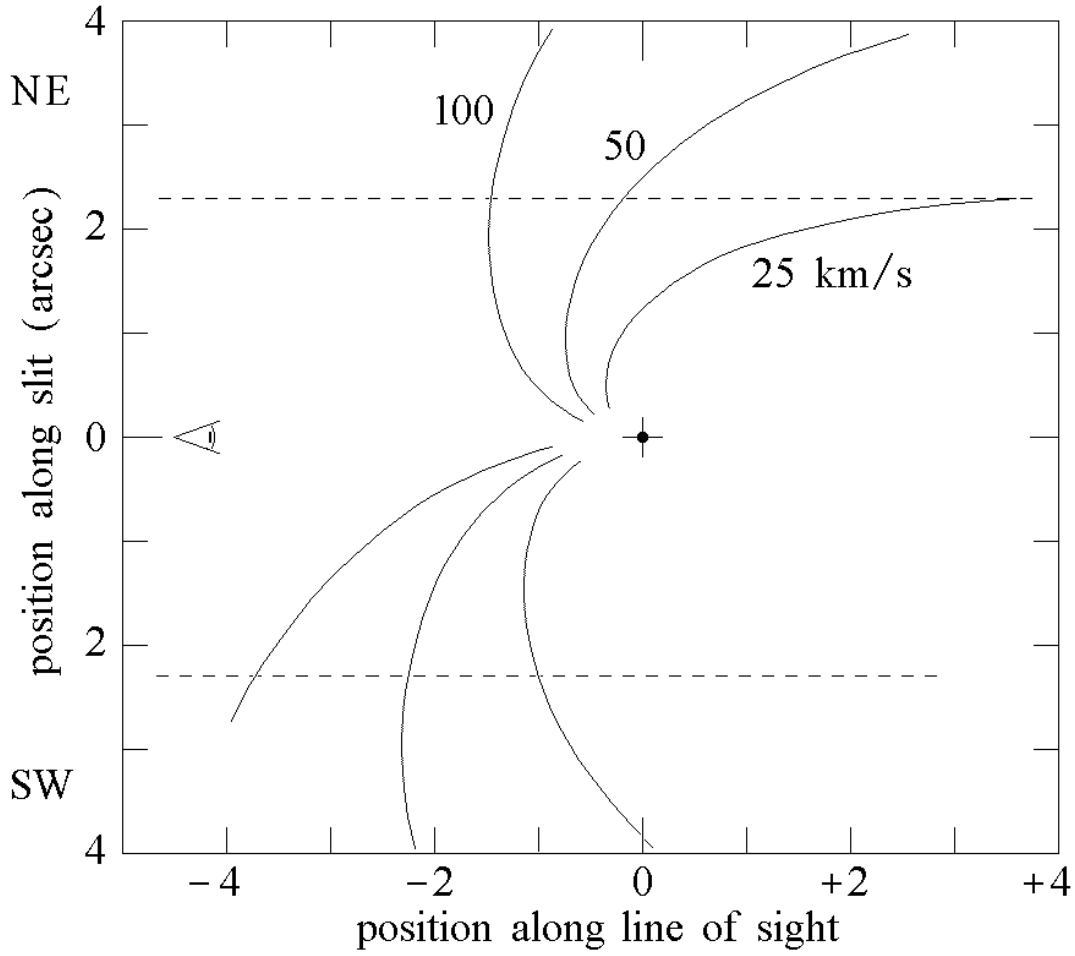

Fig. 10.— Each set of two curves shows the spatial loci corresponding to the velocity trends in Figure 9 for three different expansion velocities. Our viewpoint is to the left. The curves are not valid within 0.″5 of the center, partly because of scatter in the data there (cf. Fig. 9).

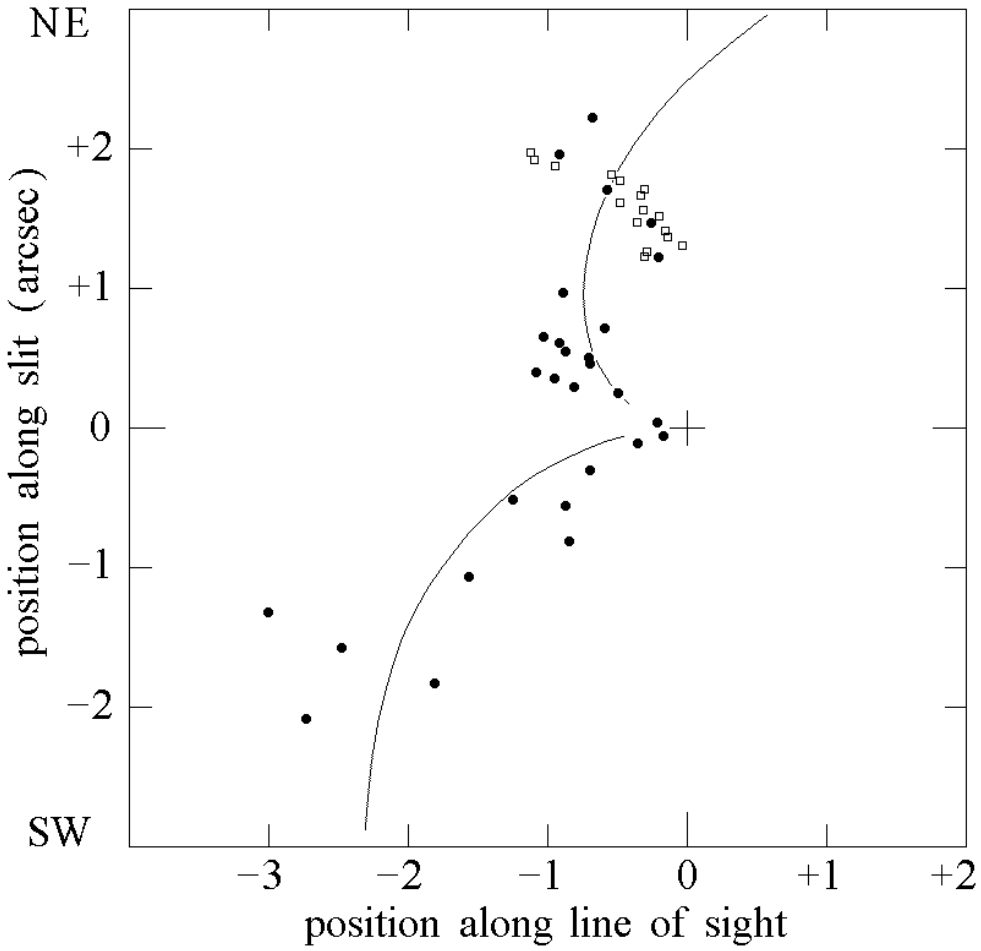

Fig. 11.— Spatial distribution of the data points in Figure 9 for $V_r = 50$ km s^{-1}. The symbols are the same as in Figure 9.

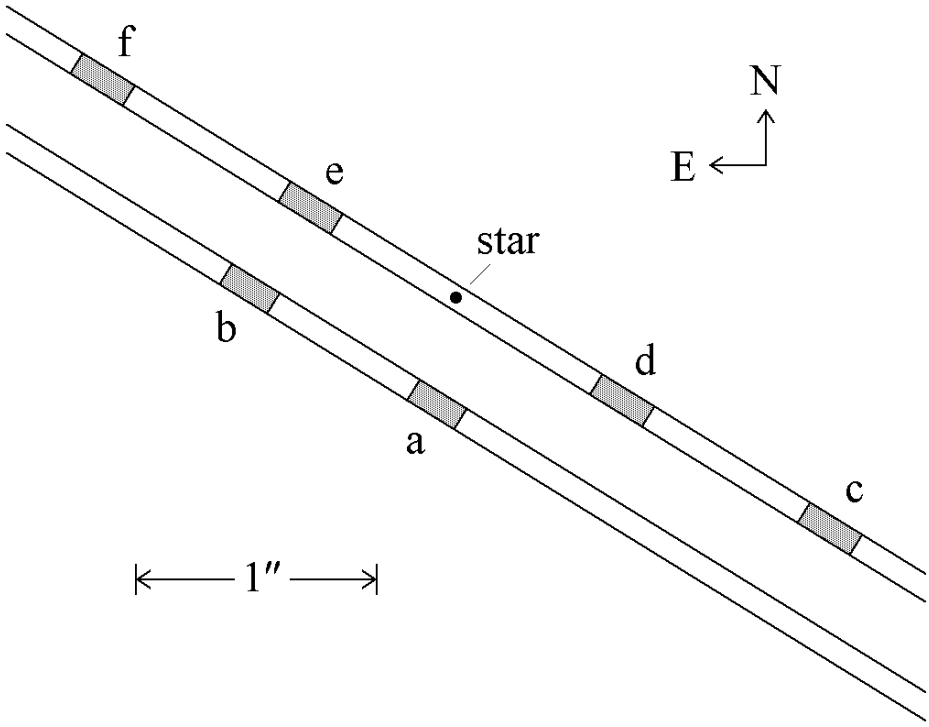

Fig. 12.— Map of the 6 positions used to sample the Hα profile.

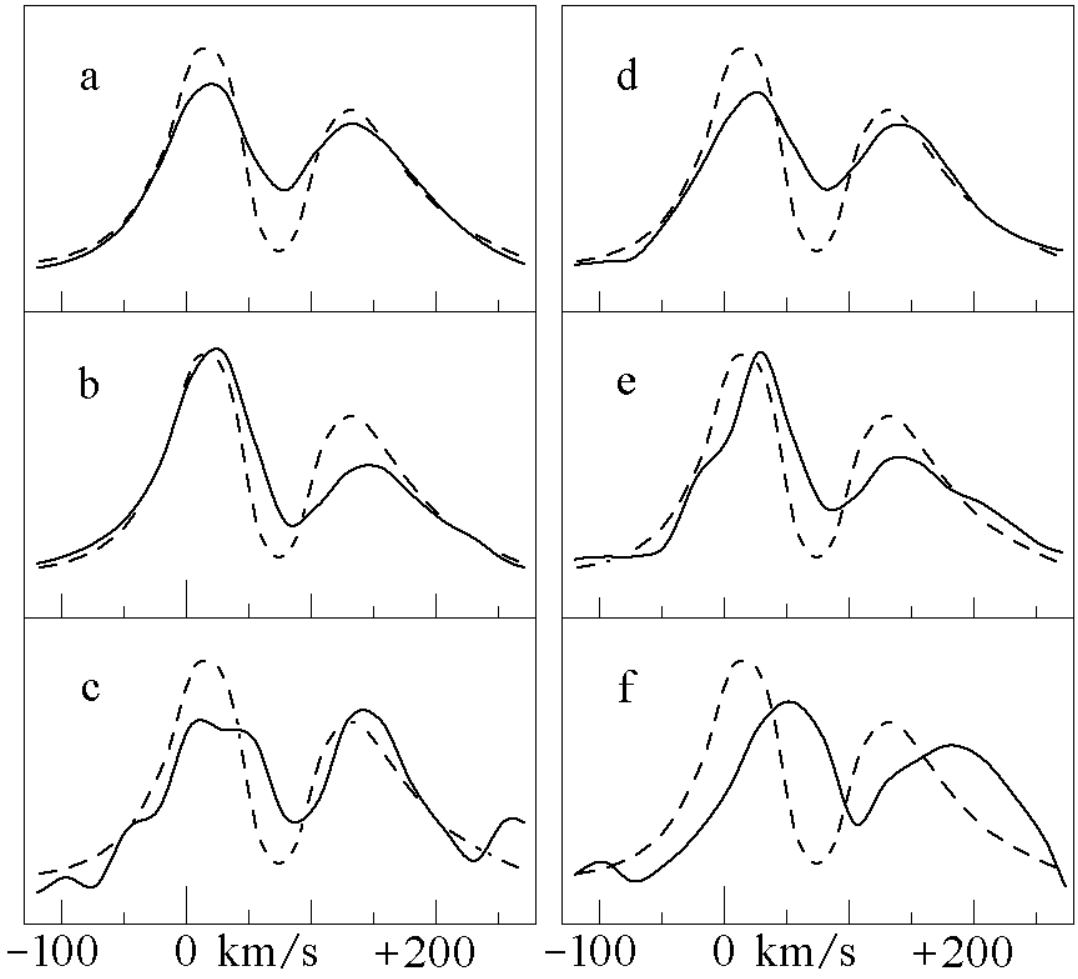

Fig. 13.— The Hα profiles at the 6 different positions in the ejecta. For comparison, the Hα profile on the central star is shown with a dashed line.

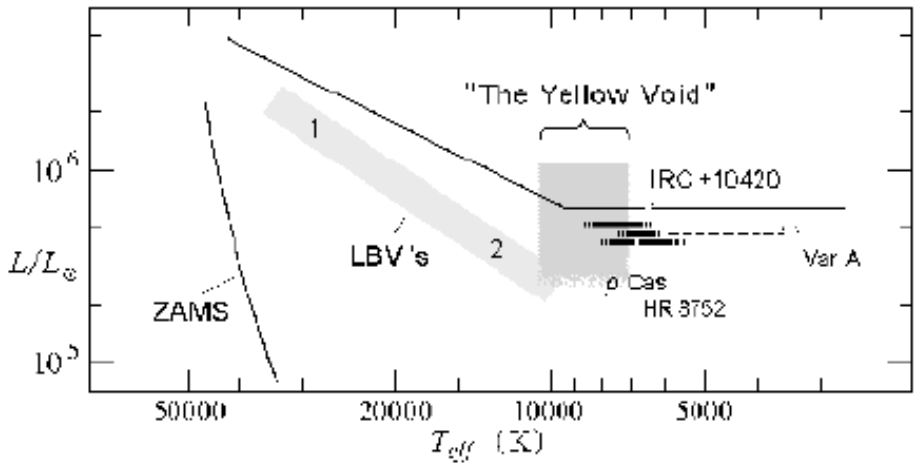

Fig. 14.— A schematic HR diagram showing the position of the yellow void with IRC +10420, Var A in M33, ρ Cas, and HR 8752 and their range in apparent temperature corresponding to their spectral variations (see text). The shell episodes in Var A and ρ Cas are shown as dashed lines. Locations of the classical (1) and less luminous (2) LBV's in their quiescent state are shown as

Table 1. Journal of HST/STIS Observations (September 10, 1999).

Grating	Slit Position	λ_c	Exp. Time(sec)	$\lambda_c/\Delta\lambda$
G750M	1	6768	8, 30, 432	6150
	2		432	
	1	7283	432	6620
	2			
	1	7795	288	7090
	2			
	1	8311	324	7560
	2			
G430M	1	4706	60, 1440	8400
	1	4961	600	8860
	2		171, 2592	

Table 2. Near-Infrared Spectroscopy .

Filter	$\lambda(\mu\mathrm{m})$[a]	$\lambda_c/\Delta\lambda$[b]
CRSP Observations, 13 June 2000		
I	0.99, 1.09	600
J	1.22	490
H	1.54, 1.66	700
K	2.22	440
PHOENIX Observations, 17 – 19 June 2000		
He I J9232	1.083	108000
Paβ J7799	1.282	94000
Brγ K4578	2.166	108000
Brα L2462	4.053	126000

[a]If two central wavelengths are given (i.e. I and H), two grating tilts were used to cover the bandpass

[b]The resolution corresponds to the 2–pixel detector resolution; for PHOENIX is actually somewhat worse, $\sim$ 75000

Table 3. Apparent Magnitudes and Colors of IRC +10420.

	Central Star		Star + halo	
Mag or Color	STIS[a]1999.7	WFPC[b]1996.3	WFPC[b]1996.3	Ground-based[c]1991
B	14.76[d]	14.6:	13.57:	13.63
V	12.18[d]	11.9:	11.06:	10.93
R_{CK}	10.45	···	···	9.56
I_{CK}	8.90	···	···	7.95
B–V	+2.58	+2.7:	+2.5:	+2.70
V–R	+1.73	···	···	+1.37
V–I	+3.28	···	···	+2.98

[a]This paper

[b]Fluxes reported in Paper II

[c]Paper I, V = 11.03 in 1994 Oudmaijer *et al.* (1996)

[d]Extrapolated or interpolated, see text and Fig. 2

Table 4. Heliocentric Velocities[a] of the Emission Lines with Split Profiles.

Line	Blue Em.	Absorption	Red Em.
Hα	14.1	72.3	134.2
Hβ	23.4	71.3	127.7
Ca II λ_{vac}8500	22.3	71.6	113.1
Ca II λ_{vac}8544	9.2	69.2	122.8

[a]To convert to LSR velocities add 17.5 km s^{-1}

Table 5. Mean Heliocentric Velocities of the Absorption and Emission Lines.

Lines	Mean Velocity	Number of Lines	Remark
Absorption Lines:			
N I	74.1 ± 4.4	10	
O I	76.1 ± 7.8	3	
Paschen lines	75.8 ± 3.9	11	
K I (stellar)	92.4 ± 5.3	2	
K I (IS)	12.7 ± 1.7	4	
Fe II,Ti II,Cr II, etc.	86.2 ± 8.5	20	
Emission Lines:			
[Ca II]	68.5 ± 1.2	2	
Permitted	67.2 ± 8.1	28	Fe II,Sc II,Y II, etc.
Forbidden	64.4 ± 7.9	8	Fe II,V II,Cr II, etc.
Neutral(Fe I)	68.7 ± 10.2	3	
Neutral(K I, slit 2)	61.0 ± 3.2	2	
Inverse P Cygni Profiles:			
Emission	40 ± 7	13	
Absorption	107 ± 7	13	

Table 6. Additional Line Identifications in the Spectrum of the Central Star.

Element & Mult.	λ_{air}	W_λ	Hel. Vel.[a]	Notes
Absorption Lines:				
V II 29	4844.31	0.09	+84.8	1.
Emission Lines:				
Fe II (26)	4580.07	-0.21	+58.8	2.
Sc II (13)[b]	4698.28	-0.10	+68.3	1.
Ti II (48)[c]	4763.84	-0.20	+61.5	2.
Fe II (30)	4825.71	-0.04	+74.9	1.
[Fe II] (4F)	4889.63	-0.10	+64.8	blended with [Fe II] 3F, 3.
[Fe II] (3F)	4889.70		+60.5	blended with [Fe II] 4F, 3.
[Fe II] (20F)	4905.4	-0.06	+61.7	2.
[Ti II] (23F)	4925.84	-0.08	+47.5	1.
Y II (20)[d]	4982.13	-0.12	+71.4	blended with [Ti II] 23F, 2.
[Ti II] (23F)[d]	4982.73		+53.6	blended with Y II 20, 2.
[Fe II] (20F)	5005.5	-0.17	+73.4	2.
Ti II (113)	5010.20	-0.09	+61.7	1.
Ti II (113)[e]	5013.38	-0.33	+44.9	2.
[Fe II] (20F)	5020.2	-0.17	+68.1	1.
Fe II (36)	5036.92	-0.07	+82.2	2.
[Fe II] (19F)[f]	5072.40	-0.05	+38.9	2.
[Ti II] (8)	6592.93	-0.07	+78.3	1.
[Fe II] (14)[g]	7171.98	-0.11	+66.8	2.
[V II] (4F)[c]	7353.77	-0.42	+70.9	3.
[V II] (4F)	7387.5	-0.41	+63.0	1.
[Fe II] (14)[g]	7388.16	-0.36	+60.0	2.
Mn II (4)	7415.80	-0.42	+62.8	3.
[Fe II] (47)	7432.23	-0.24	+64.8	3.
[Fe II] (14)[g]	7452.50	-0.20	+64.7	2.
Fe II	7866.53	-0.14	+65.2	1.
Y II (32)	7881.90	-0.16	+57.5	2.
Fe II	7917.80	-0.06	+71.6	3.

Table 6. Table 6 – continued

Element & Mult.	λ_{air}	W_λ	Hel. Vel.[a]	Notes
Fe II	8031.32	-0.13	+60.5	3.
[Ti II] (6F)	8060.16	-0.06	+60.8	1.
[Ti II] (6F)	8085.2	-0.06	+51.8	1.
Mn II	8110.39	-0.15	+69.5	2.
Fe II	8451.00	-0.28	+74.5	1.

[a]add 17.5 km s^{-1} for LSR velocity

[b]possible blend

[c]very broad, blend

[d]very broad, blend; three peaks at lab rest wavelengths of 4981.02Å, 4981.91Å, 4982.81Å

[e]very broad, blend; two peaks at lab rest wavelengths of 5012.45Åand 5013.54Å

[f]Possible inverse P Cygni profile with neighboring absorption line which would have a velocity of +118.3 km s^{-1}. If not, then the absorption line is unidentified at lab rest wavelength of 5072.96Å

[g]Identified by Oudmaijer (1998) with [Fe I]

Note. — 1. not apparent in Oudmaijer's (1998) spectrum, 2. visible in Oudmaijer's (1998) spectrum, but not in the line list, 3. listed as unidentified in Oudmaijer (1998)

Table 7. Unidentified Lines in the STIS Spectra of the Central Star.

Measured λ	λ_{vac}	λ_{air}	W_λ	Notes
Absorption Lines:				
4698.79	4697.45	4696.13	0.04	1.
4713.70	4712.35	4711.03	0.06	2.
4714.48	4713.13	4711.81	0.09	2.
4748.77	4747.41	4746.08	0.05	1.
4787.91	4786.54	4785.20	0.04	1.
4872.22	4870.83	4869.46	0.07	1.
4909.69	4908.28	4906.91	0.21	1.
6888.96	6887.00	6885.05	0.04	1.
6957.41	6955.42	6953.47	0.08	2.
6963.53	6961.53	6959.58	0.11	2.
6973.26	6971.26	6969.31	0.08	2.
Emission Lines:				
6609.09[a]	6607.62	6605.77	-0.27	3.
6831.29	6829.78	6827.87	-0.13	3.
6858.89	6857.37	6855.45	-0.10	3.
7002.11	7000.56	6998.60	-0.17	3.
7008.10	7006.55	7004.58	-0.20	3.
7195.36	7193.76	7191.75	-0.49	1.
7268.36	7266.74	7264.71	-0.13	1.
7381.59	7379.95	7377.89	-0.24	3.
7567.85	7566.17	7564.05	-0.14	3.
7578.91	7577.23	7575.11	-0.15	3.
7676.03	7674.32	7672.17	-0.14	2.
7821.92	7820.18	7817.99	-0.10	3.
7855.63	7853.89	7851.69	-0.21	1.
7957.16	7955.40	7953.17	-0.11	3.
8078.55	8076.75	8074.49	-0.03	1.
8105.67	8103.87	8101.60	-0.05	1.
8473.70	8471.82	8469.45	-0.14	1.
8529.09[b]	8527.20	8524.81	-0.32	1.
8552.36	8550.46	8548.07	-0.35	1.
8562.14	8560.24	8557.84	-0.05	1.

[a]A broad, probably blended, emission line with peaks at 6604.67 Å and 6606.45 Å in the laboratory rest frame. A possible line identification is Sc II 6604.60 Å (19). Oudmaijer (1998) shows this feature resolved into four emission components.

[b]Broad line

Note. — 1. not apparent in Oudmaijer's (1998) spectrum, 2. visible in Oudmaijer's (1998) spectrum but not in the line list, 3. listed as unidentified in Oudmaijer (1998)

Table 8. Absorption Line Differences Between the Star and the Ejecta.

Element & Mult.	λ_{air}	W_λ star	W_λ ejecta	Remark
Fe II (42)	5018.4	0.57	0.18	
Fe II (42)	4923.9	0.60	0.03	
Cr II (30)	4824.1	0.37	0.11	
Cr II (30)	4848.2	0.25	0.15	
Cr II (30)	4864.3	0.32	0.18	
Cr II (30)	4876.4	0.33	0.24	blend
unidentified		0.11	0.015	λ6963.5, see Table 7

Table 9. Emission Line Identifications[a] in the Near–Infrared Spectra[b]

Element & Mult.	λ_{air} in microns	Comments
Mg I (27)	0.9256	blended with [Fe II]
[Fe II] (13)	0.9267	blended with Mg I
[Fe II] (13)	0.9399	blended with Mg I
Mg I (38)	0.9415	blended with [Fe II]
[Fe II] (13)	0.9471	blended with Mg I
Fe II	0.9997	
Fe II	1.0174	
[S II] (3)	1.0286	
[N I] (3)	1.0398, 1.0407	blend
[Ni II] (11)	1.0459	doubtful id.
Fe II	1.0501	
Mg I (37)	1.0811	blend
Fe II	1.0863, 1.0872	blend
Fe II	1.1125	
O I (7)	1.1287	blend
Na I (3)	1.1381, 1.1403	blend
Mg I (6)	1.1829	
[Fe II]	1.2567	
Na I (21)	1.2679	
[Fe II]	1.2703	
[Fe II]	1.3205	
[Fe II]	1.3278	
Ca II:	1.4555	blend, uncertain id
Mg I	1.5025, 1.5040, 1.5048	blend
Mg I	1.5136	blend
Mg I	1.5741, 1.5749, 1.5765	blend
Mg I	1.5880, 1.5886	blend
Mg I	1.6365	
[Fe II]	1.6435	
[Fe II]	1.6637	
[Fe II]	1.6766	
Fe II	1.6873	
Mg I	1.7109	blend with [Fe II]
Fe II	1.7338	
[Fe II]	1.7449	
Fe II	2.0600	
Na I	2.2056, 2.2077, 2.2084	blend

[a]We used Coluzzi (1993) available from the ADC and the Atomic Line List at http://www.pa.uky.edu/ peter/atomic/

[b]Not including the hydrogen lines